

## RESEARCH ARTICLE

10.1029/2019JF005254

## Infilling Abandoned Deltaic Distributary Channels Through Landward Sediment Transport

## Key Points:

- Field observations document sediment filling of a former distributary channel that was abandoned by avulsion and now accumulates sediment as the deltaic lobe recedes
- The landward transport of sediment converts a former distributary channel into a mudflat. Antecedent topography mediates deposit thickness
- The completion of distributary channel filling following an avulsion is affected by antecedent levee height and the tidal range

B. N. Carlson<sup>1</sup> , J. A. Nittrouer<sup>1</sup> , A. J. Moodie<sup>1</sup> , G. C. Kineke<sup>2</sup> , L. L. Kumpf<sup>2</sup> , H. Ma<sup>1</sup> , D. R. Parsons<sup>3</sup> , and H. Wang<sup>4</sup> 

<sup>1</sup>Department of Earth, Environmental and Planetary Sciences, William Marsh Rice University, Houston, TX, USA, <sup>2</sup>Earth and Environmental Sciences, Boston College, Chestnut Hill, MA, USA, <sup>3</sup>Energy and Environment and Institute, University of Hull, Hull, UK, <sup>4</sup>College of Marine Geosciences, Ocean University of China, Qingdao, China

**Abstract** Upon avulsion, abandoned deltaic distributary channels receive water and sediment delivered by a tie channel, overbank flow, and by tidal inundation from the receiving basin. The transport and deposition of sediment arising from this latter input have important impacts on delta development yet are not well constrained from field observations or numerical models. Herein, the Huanghe (Yellow River) delta, China, is used as a case study to evaluate how marine-sourced sediment impacts abandoned channel morphology. For this system, artificial deltaic avulsions occur approximately decadal; the abandoned channels are inundated by tides, and deposition of sediment transforms the channel into a mudflat. Field data were collected from a channel abandoned 20 yr ago and included cores that penetrated the tidally deposited mud and antecedent fluvial channel sediment, topography, bathymetry surveys, and detailed time series monitoring of hydrodynamic conditions within the tidal channel and adjacent mudflat. These data are used to validate a model that predicts the rate of accumulation and grain size of sediment delivered from the tidal channel to the mudflat. The thickness of the marine-sourced mud differs spatially by an order of magnitude and is primarily impacted by antecedent channel topography. Sediment has aggraded to an elevation approaching mean high tide, which is likely the limit of fill. As this elevation is below antecedent levees, assuming stationary relative sea level, the abandoned channel will remain a topographic low on the delta landscape and is therefore susceptible to reoccupation during future avulsions.

## Correspondence to:

B. N. Carlson,  
bc15@rice.edu

## Citation:

Carlson, B. N., Nittrouer, J. A., Moodie, A. J., Kineke, G. C., Kumpf, L. L., Ma, H., et al. (2020). Infilling abandoned deltaic distributary channels through landward sediment transport. *Journal of Geophysical Research: Earth Surface*, 125, e2019JF005254. <https://doi.org/10.1029/2019JF005254>

Received 11 JUL 2019

Accepted 10 FEB 2020

Accepted article online 11 FEB 2020

## 1. Introduction

An avulsion is the rapid abandonment of an active fluvial channel in favor of a new course (Slingerland & Smith, 2004), typically arising because sediment aggrades the channel bed more rapidly than its levees, thereby reducing cross-sectional flow area and elevating the channel relative to its surrounding floodplain (Hajek & Wolinsky, 2012; Mackey & Bridge, 1995; Mohrig et al., 2000). An avulsion usually occurs during a flood event and is facilitated by a levee crevasse that conveys water from the main channel to the floodplain, which may create a new channel or find an antecedent channel that provides enhanced flow capacity (Slingerland & Smith, 2004). Typically, input of fresh water and sediment to an abandoned channel is maintained by overbank flow of sediment-laden water during floods, as well as by tie channels, which maintain a persistent surface water connection between the primary and abandoned channels (Gray et al., 2016; Rowland et al., 2005; Toonen et al., 2012). As a result, it is possible to slowly fill abandoned channels with sediment over time (Gray et al., 2016; Toonen et al., 2012).

For most lowland fluvial systems, regional channel avulsions arise over timescales of  $10^2$ – $10^3$  yr. These events are unpredictable and rapid, so it is difficult to monitor occurrences in real time (Zinger et al., 2011). Previous studies have utilized physical experiments (Reitz et al., 2010), meander-scale avulsions in modern fluvial systems (Aalto et al., 2008; Aslan & Autin, 1999; Gray et al., 2016; Smith et al., 1989; Toonen et al., 2012), and ancient fluvial deposits preserved and exposed in rock outcrops (Chamberlin & Hajek, 2015; Mohrig et al., 2000) to gain insights about avulsion processes. For example, data from experiments and rock strata studies have the unique advantage of documenting sediment variability arising due to multiple avulsion events, whereby vertically stacked, multistory channel sand bodies separated by overbank (mud) deposits indicate reoccupation of antecedent channels. It is proposed that as a consequence of incomplete filling, abandoned channels are rendered topographic lows and remain as preferential flow paths, susceptible to reoccupation with subsequent avulsions (Chamberlin & Hajek, 2015; Mohrig et al., 2000).

The avulsion cycle and infilling of *deltaic distributary* channels, on the other hand, has received less attention. Deltaic avulsions are important as they relocate the fluvial depocenter and generate new lobes, thereby impacting the development of subaerial coastal landscape (Kim et al., 2009; Roberts, 1997). Abandoned deltaic channels, present on low-relief deltas, maintain similarities to their fluvial counterparts insofar as they may serve as preferential pathways for future avulsions (Reitz et al., 2010). Yet delta distributary channels are unique because they are impacted by waves and tides of the receiving basin, which rework and disperse sediment, eroding deltaic lobes (Nienhuis et al., 2013). For coastlines where the tidal range is large relative to typical wave heights, channel lobes may be transformed into a mudflat—that is, sediment deposits that are periodically exposed and inundated during low and high tides. The surface morphology of a mudflat evolves by spatiotemporal variation in flow velocity and sediment transport and deposition patterns. Sediment accumulation on a mudflat arises due to a spatial divergence in sediment flux, typically due to tidal asymmetries (discrepancy in flood/ebb flow velocity (Friedrichs, 2011; Le Hir et al., 2000; Mariotti & Fagherazzi, 2012)) and temporal offset of the various phases of the tidal constituents (Hoitink et al., 2003). Tidal processes can facilitate infilling of deltaic channels and, as described in previous studies, may be extensive for tidally dominated deltas or for where the tide is impacted by engineered infrastructure (Dai et al., 2016; Rahman et al., 2011; Tamura et al., 2012; Wilson & Goodbred, 2015). In general, deposit thickness and grain size diminish with distance from the tidal channel in association with these spatiotemporal variations in flow conditions. However, the degree to which the antecedent fluvial topography, including channel bars and the thalweg, influences mudflat sediment accumulation is currently unknown.

There have been few studies of the morphological development of a fluvial-deltaic lobe and associated channel upon abandonment by avulsion. The Huanghe (Yellow River) delta of China offers an intriguing study site: Multiple abandoned lobes persist across the delta as a consequence of major channel avulsions occurring on a decadal timescale, largely due to engineered diversions (Figure 1). The long-term outcome is that these former channels and lobes are transformed into mudflats; however, this process, as related to the impacts of waves and tides, is not well understood. For mudflats, flood tides route sediment-laden water from a tidal channel over the adjacent mudflat: Water velocity in the tidal channel exceeds that of the open mudflat, and so the dominant direction of particles is directed toward the mudflat during flood tide. Deposition occurs during slack high water, when water velocity is sufficiently low for settling of fine sediment (Friedrichs, 2011; Mariotti & Fagherazzi, 2011; Mariotti & Fagherazzi, 2012; Van Maren & Winterwerp, 2013). A scour lag—defined as the excess shear stress required to entrain fine (cohesive) particles relative to the shear stress required to keep those particles in suspension—combined with lower shear stress over the mudflat during ebb tide prevents remobilization of deposited materials and facilitates sediment accumulation (Ridderinkhof et al., 2000). An additional factor, settling lag, occurs when there is a delay in deposition after the flow velocity and energy dissipate to a level that is no longer capable of maintaining sediment in suspension. Moreover, as tidal velocity decreases landward and slack duration is longer for high tides landward deposition of sediment is facilitated (Postma, 1961; Van Straaten & Kuenen, 1958).

Herein, the infilling of a fluvial-deltaic channel abandoned after an avulsion, and the conversion of this channel into a mudflat, is assessed by evaluating the relative role of tides and storms for different seasonal conditions. The source of sediment to the mudflat is constrained through detailed grain size and fluid property measurements, and deposit thickness is contextualized based on antecedent channel topography. Field data are sourced from the abandoned Qingshuigou lobe of the Huanghe delta, which was active from 1976–1996. The Qingshuigou lobe was abandoned through engineering practices that completely cut off upstream water and sediment supply; therefore, the role of tides and waves for sediment delivery can be isolated from other complicating factors, such as fluvial and estuarine processes. The role of receiving basin hydrodynamics is evaluated in regard to the evolution of this distributary channel. These factors directly impact the propensity for a channel to completely anneal or persist as a topographic low on the fluvial-deltaic landscape and therefore remain a possible site of fluvial channel reoccupation.

## 2. Regional Setting

Sourced from the Tibetan Plateau, the Huanghe traverses the North China Plain, carrying predominantly silt-sized sediment, and debouches into the Bohai Sea where it builds the Huanghe delta (Yu, 2002; Zhang

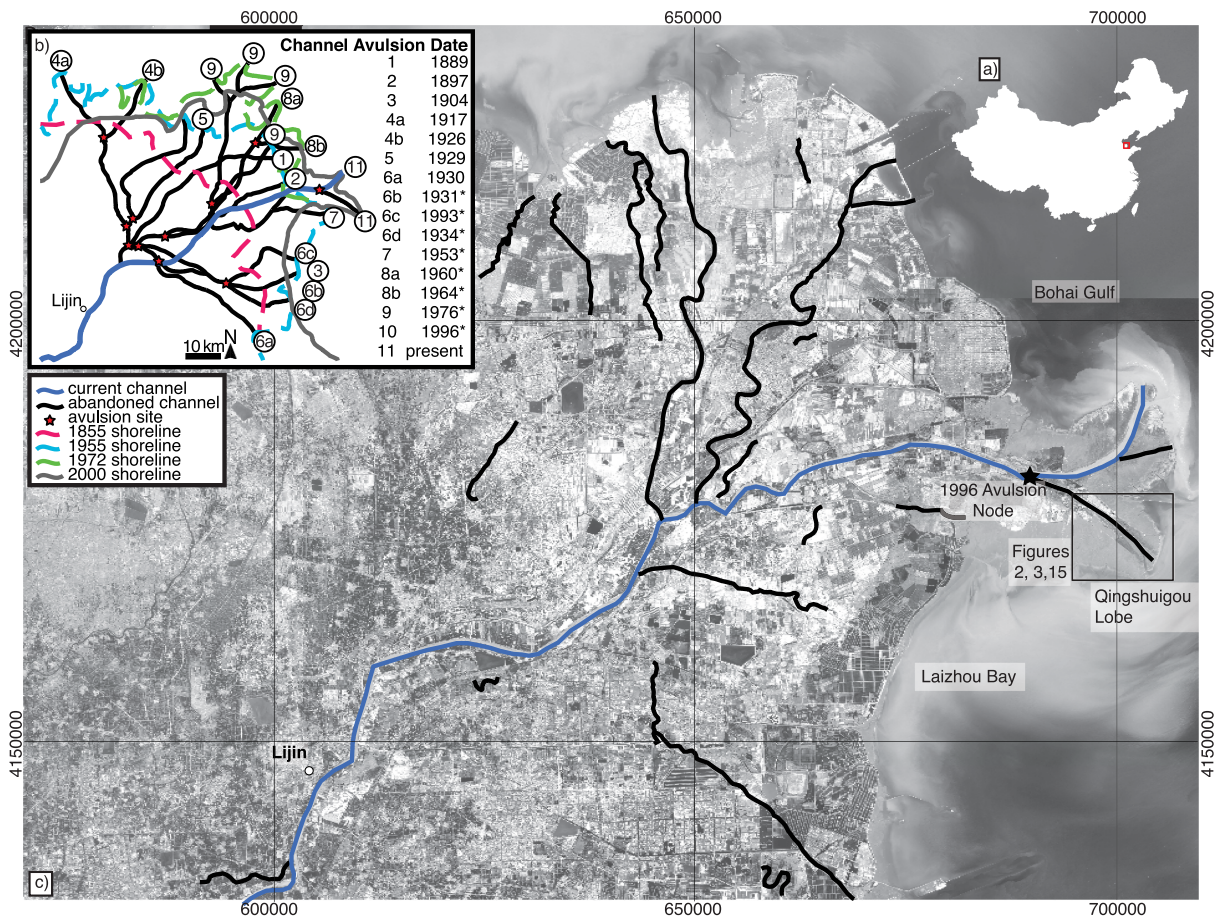


**Figure 1.** (a) Map of China, denoting the location of the Huanghe delta (within red square), which builds into the Bohai Sea. (b) The Huanghe delta, which avulses every decade by abandoning an active channel in favor of a new pathway to the sea, which presently occurs through both natural processes and engineering practices. The active channel is represented by the blue line, and black lines locate prior channels (modified from (Chu et al., 2006; Pang et al., 1979; Saito et al., 2000; Van Gelder et al., 1994). (c) Composite Sentinel-2 image assembled from images spanning November 2017 to June 2018. Currently, some abandoned channel pathways are visible on the landscape; however, others are annealed (topographic lows that have subsequently filled with sediment). The Qingshuigou lobe was abandoned through engineering practices in 1996, and the node location is denoted by the black star. A tidal channel delivers water and sediment to the mudflats that occupy the abandoned Qingshuigou channel and lobe.

et al., 1990). Sediment and water discharge vary seasonally, where peak flow conditions occur during summer months, and low flow conditions occur during winter months (Wang & Liang, 2000). High sediment loads (exceeding 1 Gt/yr) and low water discharge ( $427 \times 10^8 \text{ m}^3$  annually) of the Huanghe yield a high sediment concentration that leads to enhanced morphodynamics relative to most other deltaic systems (Ma et al., 2019; Yu, 2002). For example, approximately every decade the Huanghe abandons a deltaic lobe to construct a new one through both natural and engineered avulsions (Ganti, Chu, et al., 2014; Van Gelder et al., 1994). Hence, the delta is a composite of numerous lobes that have developed over the past century. Interestingly, the Huanghe maintains a single-channel lobe, that is, there are no major natural bifurcations of the primary channel approaching its receiving basin, and it has classically been considered a river-dominated delta (Galloway, 1975). The lower Huanghe bankfull flow depth ranges 2–5 m, and the channel bed slope ranges  $8.8 \times 10^{-5}$  to  $1.0 \times 10^{-4}$ , yielding a backwater length that ranges 21–54 km (Ganti, Chu, et al., 2014; He, 2019). The Huanghe widens near the mouth, which is typical of rivers that are influenced by tides (Galloway, 1975).

The Bohai Sea influences the Huanghe delta lobes in several ways. The coast of the Huanghe delta is flanked by extensive tidal flats, which are predominantly composed of mud (Shi et al., 2017). Astronomical tides are mixed semidiurnal, and microtidal to mesotidal, with a range of 0.6–0.8 m near the river mouth and 1.5–2 m

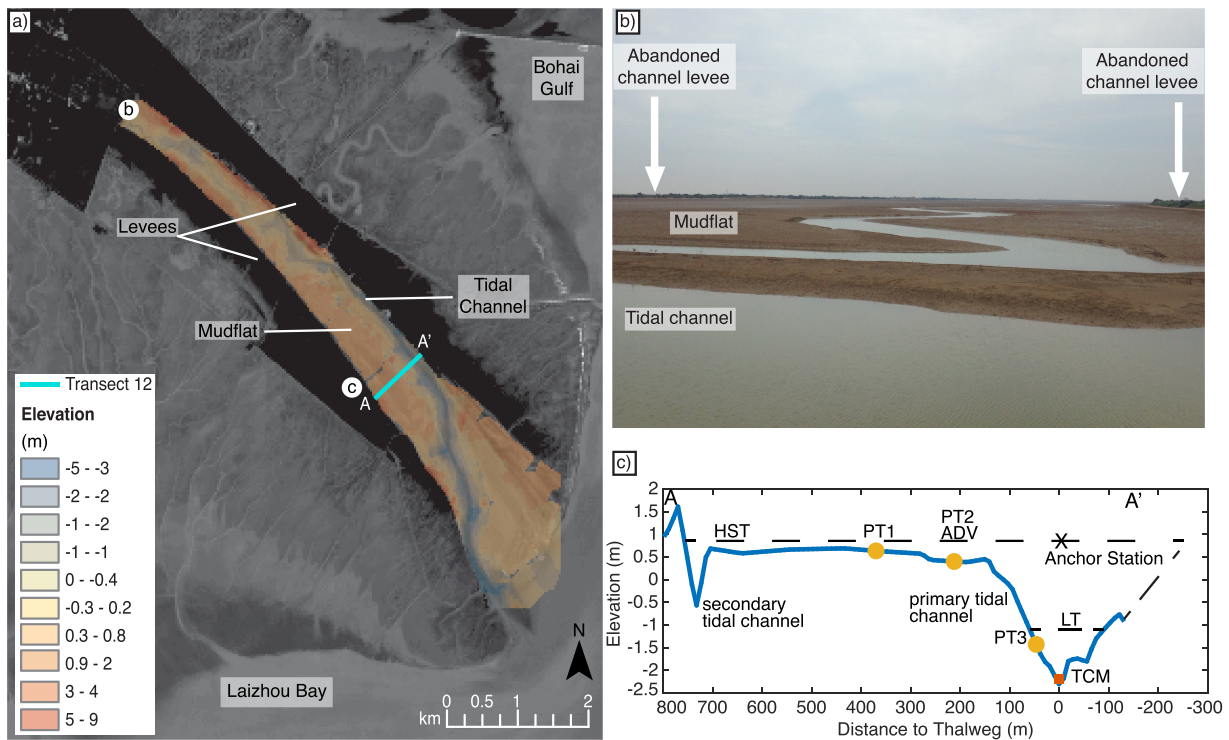


**Figure 2.** (a) Elevation of the Qingshuigou channel and lobe, referenced to mean sea level. (b) A photograph of the abandoned Qingshuigou channel, looking downstream, approximately 10 km from the Bohai Sea. Note the abandoned Huanghe levees, visible by occurrence of vegetation, which are ~600 m apart (i.e., width of the antecedent channel). A tidal channel and mudflat now occupy the abandoned channel. (c) Transect 12 elevation cross section (location shown in (a)), where monitoring instruments were deployed and where the 25-hr measurement station observations were collected to measure hydrodynamic and sediment conditions. The highest water level recorded at spring tide is labeled “HST,” and the lowest water level recorded is labeled “LT.”

in the north Bohai Gulf and to the south in Laizhou Bay (Zhang et al., 1990). Associated current velocity is 1–2 m/s (Wang et al., 2010). A seasonal wave climate also impacts sediment transport. During summer months, southerly winds produce small significant waves heights (0.3–0.7 m), and during winter months, strong northeasterly winds from the East Asian Winter Monsoon (EAWM) generate significant wave heights exceeding 4 m (Wang et al., 2014). Hence, seabed sediment resuspension in the Bohai Sea is common during winter months (Wang et al., 2014).

Most of the abandoned distributary channels of the Huanghe delta have been partially, if not entirely, filled with sediment (Figure 1) (Chu et al., 2006; Pang & Si, 1979; Saito et al., 2000; Van Gelder et al., 1994). The particular lobe and channel that is the focus of this study is the Qingshuigou lobe (Figures 1 and 2). When the Qingshuigou lobe was active, the subaerial deposit rapidly prograded into the Bohai at a rate exceeding 1 km/yr (Chu et al., 2006; Moodie et al., 2019; Wright & Nittrouer, 1995). Winter storms were highly effective at suspending sediment delivered to the delta front, and these storms redistributed sediment along the coastline via wave- and wind-driven currents and downslope by way of gravity flows and slope failures (Wright & Nittrouer, 1995; Wright et al., 1986). In July of 1996, an engineered avulsion rerouted this distributary channel ~20 km to the northeast. As a consequence of the engineered design, there was no upstream input of sediment or riverine water to the abandoned channel. The bed resides at an elevation that renders it intertidal and thus subject to periodic inundation. Over the last 20 yr, the fluvial channel has converted into a mudflat, which currently maintains one primary tidal channel (Figure 2). The former levees of the Qingshuigou channel are presently situated up to 1.5 m above the high high tide elevation, and so tidal flows are contained by this antecedent topography. As a consequence of little freshwater input (except atmospheric precipitation), and high evaporation potential in the summer months, the abandoned Qingshuigou lobe mudflat maintains high salinity. The only vegetation to occupy the mudflat—*suaeda salsa*—tolerates these hypersaline conditions.

### 3. Materials and Methods

Field observations and a modeling framework are presented in this section. The field survey was designed to capture the major driving factors and processes that result in sediment accumulation within the Qingshuigou abandoned channel. A topographic survey was conducted to constrain boundary conditions for not only the fluid flow and sediment transport regimes but also the sedimentological and morphological impacts of tides and waves at the field site. Field observations inform a simplified model that captures the primary parameters necessary to predict sediment transport for an abandoned deltaic distributary channel filling with exclusively marine-derived sediment.

#### 3.1. Topographic Survey

Elevation data were collected during summer field surveys of 2016 and 2017 (Figure 2). In 2016, total station survey measurements were collected along transects oriented transverse to the abandoned channel, spaced 500 m apart. Along the transects, elevation data were collected by survey points that were located based on the local elevation variation: Points were spaced approximately 10 m where it was relatively flat and 1–5 m where topography change was evident (e.g., tidal channel banks and channel beds). Several elevation benchmarks located 2.6–3.2 km northeast of the most landward position of the survey were used to reference the survey data to the Huang Hai elevation datum (Zhang et al., 2012). In 2017, the abandoned channel was surveyed with real-time kinematic (RTK) differential GPS survey equipment. Transects were spaced 1 km apart, coinciding with transects collected in 2016. The total station data collected in 2016 have a horizontal error of 0.02–0.09 m and a vertical error of 0.02–0.05 m, which increases with distance from the benchmark (i.e., the error propagates seaward). The RTK data have a horizontal error of 0.001 m and a vertical error of 0.0015 m.

A bathymetric survey was conducted within the main tidal channel in 2016 using a single-beam echo sounder (Lowrance, HDS-7). Data were collected at ~10 m spacing, and the survey covered areas of the channel that were too deep to wade for the total station and the RTK GPS survey. These bathymetric data were also referenced to the Huang Hai elevation datum using a pressure transducer located at a known elevation in the tidal channel.

#### 3.2. Sedimentological Data

During two campaigns (summer 2015 and 2016), a series of cores and pits were excavated within the abandoned channel. Seventeen 6-m-long vibracores were obtained from the abandoned channel mudflat during the 2015 campaign (Figure 3). A depth of 6 m was chosen to ensure penetration into the sediments that comprised the antecedent channel bed, which maintained a thalweg depth of ~1–4 m (Van Gelder et al., 1994; Wang & Liang, 2000). Seven coring transects oriented transverse to the channel were spaced 1 km apart in the downstream direction. Three cores were extracted per transect, located on the right bank, left bank, and channel center. Cores were opened with a circular disk saw, described, and imaged. Samples were collected every 0.05 m in silt and clay packages and 0.2 m in the sand packages. In 2016, 45 pits were excavated to provide increased spatial resolution of the shallow stratigraphy. Five pits were dug per transect (established during the 2015 campaign, Figure 3). Pits were dug to the water table (~50 cm), which was usually adequate to resolve the sand-mud contact, interpreted to be the fluvial-to-tidal sediment transition (see below). Pits were described, taking note of grain size transitions (abrupt vs. gradual). Samples were collected from the pits at 10-cm intervals. Grain size data for the core and pit samples were obtained by laser particle diffraction analysis using a Malvern Mastersizer 2000.

#### 3.3. Tidal Channel Observations

In summer 2017 and winter 2018, a suite of instruments were deployed within the tidal channel to continuously monitor water velocity and depth. A Lowell Tilt Current Meter (TCM-1), which contains a three-axis accelerometer and three-axis magnetometer for measuring instrument tilt and bearing, was used to measure flow velocity. The instrument collected measurements at 1-min intervals, and the resulting orientation data were converted to current velocity (considered the average value over the of the 75-cm-long instrument). Water depth in the primary tidal channel was measured using an Onset HOBO pressure transducer (PT3) logging at 5-min intervals. Measurements were corrected for barometric pressure using data collected from a PT placed in a nearby tree. Readings were converted to water surface elevation above the transducer assuming hydrostatic conditions and a saline water density ( $1.025 \text{ g/cm}^3$ ) (Fitts, 2002). PT3 was placed such that it was continuously submerged throughout the field campaign.

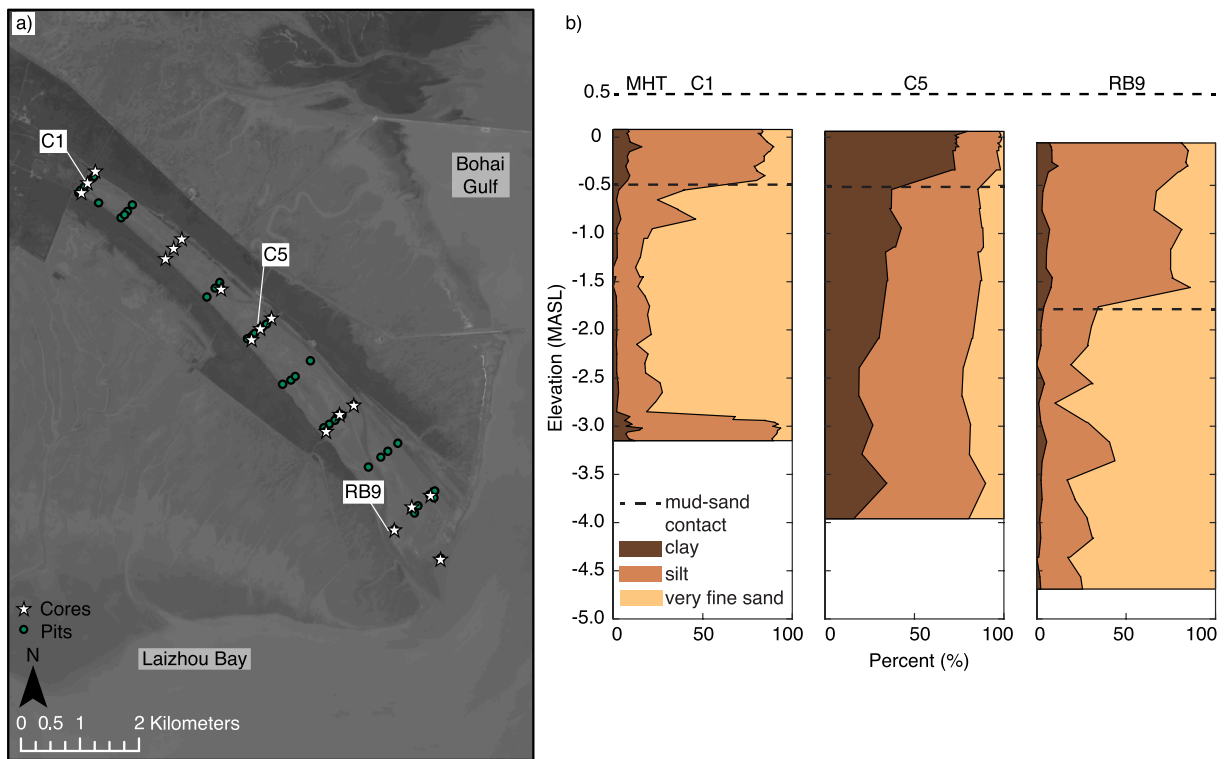


**Figure 3.** (a) Map indicating the location for the seventeen 6-m-long vibracores (white stars) and 45 pits excavated in the Qingshuigou lobe. (b) Grain size of sediment collected in three cores, showing proportion of clay, silt, and sand, referenced to depth below the surface. “MHT” indicates the elevation of the mean high tide in meters above sea level (MASL). Note that mud dominates the shallower portion, while silt and sand fractions increase with depth.

During both the 2017 and 2018 field campaigns, shipboard (anchor) measurement stations were conducted at astronomical spring tide. Within the tidal channel along Transect 12 (T12) (Figure 2), the summer measurement station was 25 hr and the winter measurement station was 13 hr. Shipboard measurements of velocity profiles, suspended sediment, and near-bed velocity measurements were collected. Flow depth was continuously recorded using a Lowrance HDS-7 echo sounder, equipped with two dual frequency sonar heads, which provide downward single-beam sonar (50/200 kHz) as well as side-scan sonar (455/800 kHz). Velocity profiles were recorded during measurement stations using an acoustic Doppler current profiler (ADCP) recording at 2 Hz. The ADCP measurements were usable up to 0.25 m from the channel bottom due to reflection off the bed, so a mechanical velocimeter (Swoffer 3000) was deployed to measure near-bed velocity at 0.05, 0.15, 0.30, and 0.75 m above the bed at 30-min intervals. Near-bed water samples were collected at 0.092 m above the channel bed every 30 min using an in situ pump system mounted on an instrumented tripod that could be lowered to and rest on the channel bed (Sternberg et al., 1991). These samples were analyzed for near-bed suspended sediment concentration (SSC) values. Water samples from the top ~0.2 m of the water column that were obtained every hour with a bucket were used to determine surface SSC using standard filtration, drying, and weighing techniques. Channel-bed sediment samples were collected at 30-min intervals using a Petite Ponar Sampler and also subsequently analyzed for grain size distribution using the Malvern Mastersizer 2000.

### 3.4. Mudflat Observations

Water depth and velocity were continuously monitored on the mudflat during the summer 2017 and winter 2018 field campaigns. Two PTs were deployed along T12 (i.e., PT1, PT2; Figure 2) in an arrangement that covered the entire tidal elevation range on the mudflat when including PT3. The two PTs that were deployed on the mudflat were located at 178 m (PT2) and 331 m (PT1) from the channel bank (Figure 2). The mudflat elevations are intertidal, and so PT1 and PT2 were not always submerged. PT measurements were collected every 5 min for 24 days in the summer and 20 days in the winter. Readings were subsequently corrected for

atmospheric pressure and converted to water depth assuming hydrostatic conditions and a saline water density ( $1.025 \text{ g/cm}^3$ ).

An Acoustic Doppler Velocimeter (ADV) was colocated with PT2 and provided point measurements of velocity 0.16 m above the mudflat. The ADV is measured at 16 Hz for 10 s at 30-s intervals; however data are only available when the ADV is inundated with water (i.e.,  $>0.36 \text{ m}$  above the mudflat bed). Data collected by the ADV are subject to the quality control standards outlined in Elgar et al. (2005).

### 3.5. Analytical Framework for Suspended Sediment in the Tidal Channel

Shear stress induced by tidal currents drives the suspension of sediment from the tidal channel bed. At rising tide, sediment-laden water emerges from the tidal channel and inundates the adjacent mudflat. Sediment deposition occurs as particles settle from the water, as is expected with slowing flow velocity onto the mudflat and especially with slack tide conditions (Friedrichs, 2011). Both SSC and grain size distribution for the part of the water column that inundates the mudflat can be analyzed using a model that predicts grain size specific concentration profiles. Here the formulation of this model is described.

The vertical SSC profile for the tidal channel for a grain size,  $i$ , is given by:

$$\frac{c_i}{c_{bi}} = \left[ \frac{(H-Z)/Z}{(H-b)/b} \right]^{P_{Ri}}, \quad (1)$$

where  $c_i$  is the concentration of the  $i$ th grain size evaluated at an elevation  $Z$  above the bed, where  $H$  is the total flow depth, and  $P_{Ri}$  is the Rouse number (Rouse, 1937):

$$P_{Ri} = \frac{w_{si}}{\kappa u_*}. \quad (2)$$

$w_{si}$  is the settling velocity of the  $i$ th grain size, where settling velocities for particles that exceed  $16 \mu\text{m}$  are determined by Dietrich (1982) and particles less than  $16 \mu\text{m}$  are assumed to be flocculated and are assigned a  $w_s$  of  $1 \text{ mm/s}$  (Smith & Friedrichs, 2011; Warner et al., 2008).  $\kappa = 0.4$  is the dimensionless von Kármán constant,  $u_*$  is the shear velocity, and  $b$  is the top of the bedload layer (Wiberg & Rubin, 1989):

$$\frac{b}{D_{50}} = \frac{A_1 T^*}{1 + A_2 T^*}, \quad (3)$$

where  $A_1 = 0.68$  and  $A_2$  is a function of the median grain diameter of bed sediment,  $D_{50}$ :

$$A_2 = 0.0204(\ln D_{50})^2 + 0.022(\ln D_{50}) + 0.0709,$$

and  $T^*$  is the dimensionless ratio:

$$T_i^* = \frac{\tau_b}{\tau_{ci}}, \quad (4)$$

where  $\tau_b = \rho u_*^2$  is the boundary shear stress,  $\rho = 1.025 \text{ g/cm}^3$  is the water density, and  $\tau_c = 0.03$  is the critical shear stress of grain mobility and is fixed for all grain sizes. A single value for  $\tau_c$  is used because the bed sediment possesses a particle size range that is cohesive (clay and silt), and therefore, a single-particle entrainment function may not be appropriate. Recent studies have shown that multiparticle aggregate entrainment is common for silt (Van Maren et al., 2009).

The sediment concentration at the top of the bedload layer is computed using the McLean (1992) entrainment relationship:

$$c_{bi} = F_i \frac{0.004(1-\varphi)E_i}{1 + 0.004E_i}, \quad (5)$$

where  $F_i$  is the fraction of grain size  $i$  of the total distribution,  $\varphi = 0.35$  is the sediment bed porosity, and  $E = T^* - 1$  is the transport stage. The individual grain size specific concentration profiles are summed to produce a complete concentration profile.

Model inputs for equations (1)–(5) are constrained through field observation and include (1) grain size distribution of bed material, (2) flow depth ( $H$ ), and (3) shear velocity ( $u_*$ , determined by fitting a law-of-the-wall logarithmic velocity profile to mechanical velocimeter data; e.g., Garcia (2008)). Bed material entrainment is calculated for 35 discrete logarithmically spaced grain size classes ranging 1–350  $\mu\text{m}$  for three  $u_*$  values (20th, 50th, and 80th percentiles of measured  $u_*$ ). Volumetric SSC and grain size distribution are calculated at 0.04-m intervals. The model is evaluated for each tidal channel bed sample collected in order to characterize a range of possible SSC profiles. The finest bed sample distribution will generate maximum SSC, and the coarsest bed sample distribution will generate the lowest predicted SSC.

## 4. Results

### 4.1. Elevation and Bathymetry

The elevation and bathymetry data reveal that the tidal channel in the Qingshuigou abandoned channel deepens and widens as it approaches the Bohai Sea (Figure 2a), reaching a depth of  $\sim 5$  m near the shoreline of the abandoned deltaic lobe. No expression of tidal channel levees is discernible from the elevation data. The seaward dipping slope of the tidal channel bed is  $2 \times 10^{-4}$ , and the mudflat dips seaward with a slope of  $9.8 \times 10^{-5}$ . The old levees of the Qingshuigou lobe are up to 1.5 m above the mudflat surface, with the highest relief located landward and a steady decrease toward the Bohai Sea (Figure 2).

### 4.2. Sedimentological Data

Of the 17 extracted cores, nine display an abrupt contact between a thick ( $\sim 5$  m) silty sand package and an overlying mud deposit  $\sim 0.3$ – $1.8$  m thick (Figure 3). Eight cores display mud and sand interbedded and maintain an overall fining upward trend. For cores that penetrated to 6 m, the bottom typically displays interbedded mud and sand (Figure 3). For all cores, silty sand packages are massive (meters thick), with intervals of shallow-dipping fore sets; however, no fine stratigraphy is observed, as the operation of the vibro-core likely perturbed small structures.

Of the 45 pits that were excavated, a mud-sand contact was resolvable in 25, with an average depth of the mud-sand contact located at 0.19 m below the mudflat surface. In six pits, where the mud-sand contact was not reached before encountering the water table, this contact is assumed  $>0.40$  m below the surface. For pits near the tidal channel, there is often no obvious mud-sand transition. Instead, a mud layer caps centimeter-scale mud and sand laminae that lack sedimentary structures (14 pits). Generally, far from the tidal channels ( $>60$  m), it is possible to identify an abrupt mud-sand contact. Mud thickness, grain size (50th and 90th percentiles), and sorting were examined as a function of distance from the primary tidal channel centerline (Figure 4a) and with distance from the shoreline (Figure 4b). No spatial trends in thickness, grain size, or sorting are discernible.

Grain size distributions from massive sand deposits in the cores were compared to bed sediment samples collected from the active Huanghe channel (Ma et al., 2017). A two-sample Kolmogorov-Smirnov (K-S) test (Figure 5a) shows that the grain size distributions are likely from the same continuous distribution with a 95% confidence level. A two-sample K-S test was also used to compare randomly chosen core samples to randomly chosen active channel bed samples (Figure 5b). For 69% of the tests, the two samples are likely from the same continuous distribution, while 31% reject that the samples are from the same continuous distribution, at a 95% confidence level.

### 4.3. Tidal Channel Observations

#### 4.3.1. Summer 2017

The highest tidal range recorded by the PT in the tidal channel was 1.6 m (Figure 6a), coinciding with spring tide. Tides are mixed near spring tide (i.e., larger range between lower high and high high tide, Figure 6a). At neap tide, the tidal range is 1 m, and the tides are less mixed (i.e., smaller range between lower high and high high tide, Figure 6a). The TCM-1 located at T12 recorded near-bottom velocity up to 1 m/s, occurring during an ebb flow of spring tide (Figure 6b).

During a 25-hr observation period, measurements were collected over a spring tide. The median grain sizes for the seven samples collected from the tidal channel bed during the measurement station are 42–78  $\mu\text{m}$  (Figure 6d). Water depth in the channel is 0.9–2.5 m (Figure 7a). Depth-averaged velocity recorded by the ADCP is up to 1.1 m/s (Figure 7b), with the fastest velocity recorded during ebb flow. Near-bottom

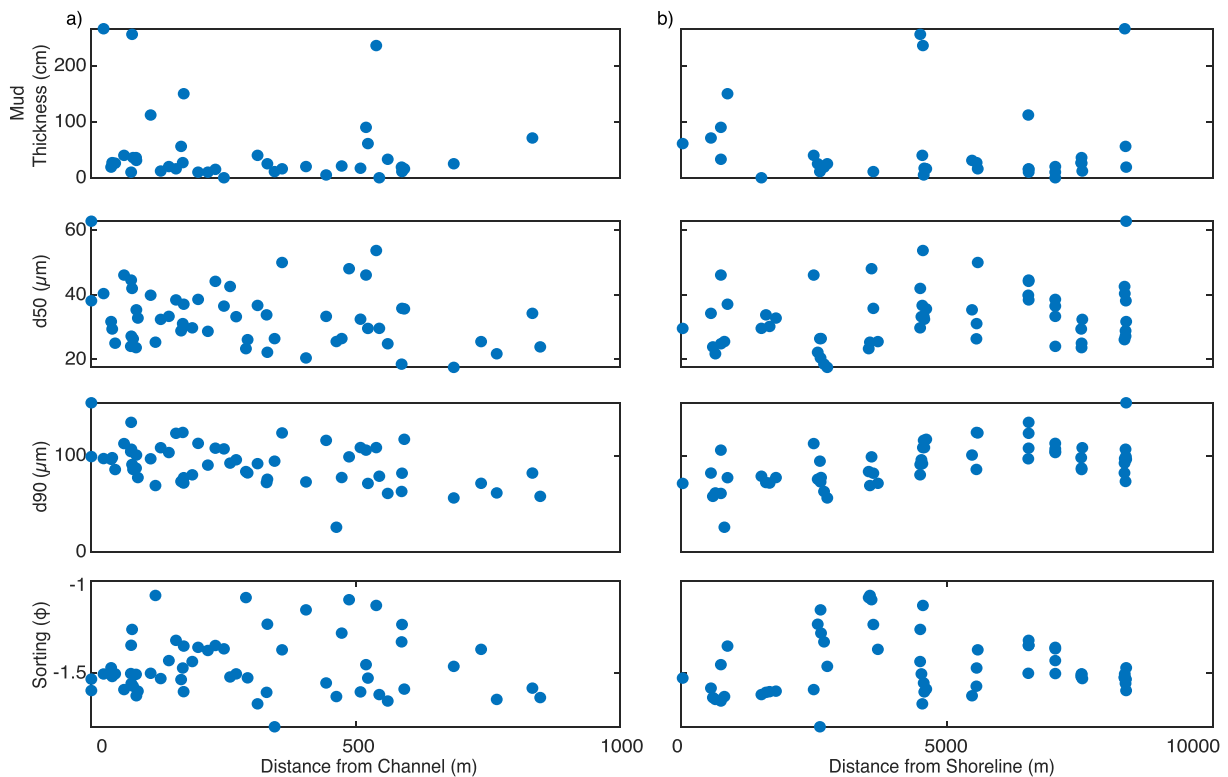


**Figure 4.** (a) Mud thickness, median grain size (D50), 90th percentile coarsest sediment (D90), and sediment sorting for surface samples, plotted with respect to distance from the primary tidal channel (i.e., transverse to tidal channel axis). No spatial trends are evident from the data. (b) Mud thickness, D50, D90, and sediment size sorting for surface samples, plotted with respect to distance from the 2016 shoreline determined in a Landsat 8 image. Mud thickness is variable over this distance, and sorting, D50, and D90 are relatively consistent, with the data displaying no trend.

velocity collected using the mechanical velocimeter ranges up to 0.9 m/s. These data are used to estimate shear velocity,  $u_*$ , assuming a law-of-the-wall relationship (Figure 7c). Near-bottom SSC measurements are  $2 \times 10^1$  to  $2 \times 10^3$  mg/L (Figure 7d), and the surface sediment concentration measures  $1.5 \times 10^1$  to  $5.8 \times 10^2$  mg/L (Figure 7d). The highest concentration measured for both the near-bottom and the surface samples corresponds to the highest recorded velocity and shear stress. Furthermore, the near-bottom SSC data and  $u_*$  estimates exhibit a correlation of  $R^2 = 0.76$  when the data are fit with a nonlinear model using the Rouse equation, allowing  $c_b$  and  $w_s$  to be free parameters (Figure 8). The surface SSC data and the estimated  $u_*$  values are found to be correlated with an  $R^2$  value of 0.83 when fitted with the functional form of the Rouse profile (Figure 8).

#### 4.3.2. Winter 2018

Pressure transducer data collected within the tidal channel document a tidal range of 0.6–2.7 m. The lowest range is associated with a neap tide, while the highest range is associated with an EAWM wind event compounded with a spring tide (Figure 6e). The TCM velocity data show that the highest velocity in the channel occurs during storm events and high high spring tide, with the maximum velocity recorded during ebb flow (1 m/s). The lowest velocity occurs during fair weather and neap conditions at slack tide (Figure 6f). Water depth in the tidal channel is strongly correlated to high wind velocity directed from the northeast (Figure 9). At the onset of winter storms, wind velocity is 35–40 kph, and water elevation achieves a maximum value during the observation period (i.e., ~2 m). With the cessation of high wind, water depth decreases, yet the spring/neap signatures remain obscured (Figure 9).

A 13-hr measurement station was conducted 1 day after a large northeasterly wind event. At the onset of the wind event, the mudflat was inundated with 1.20 m of water. However, throughout the measurement station, no inundation occurred on the mudflat. Furthermore, water depth was too low to collect resolvable ADCP data. The mechanical velocimeter measured near-bed velocity up to 0.3 m/s. During the storm event, the

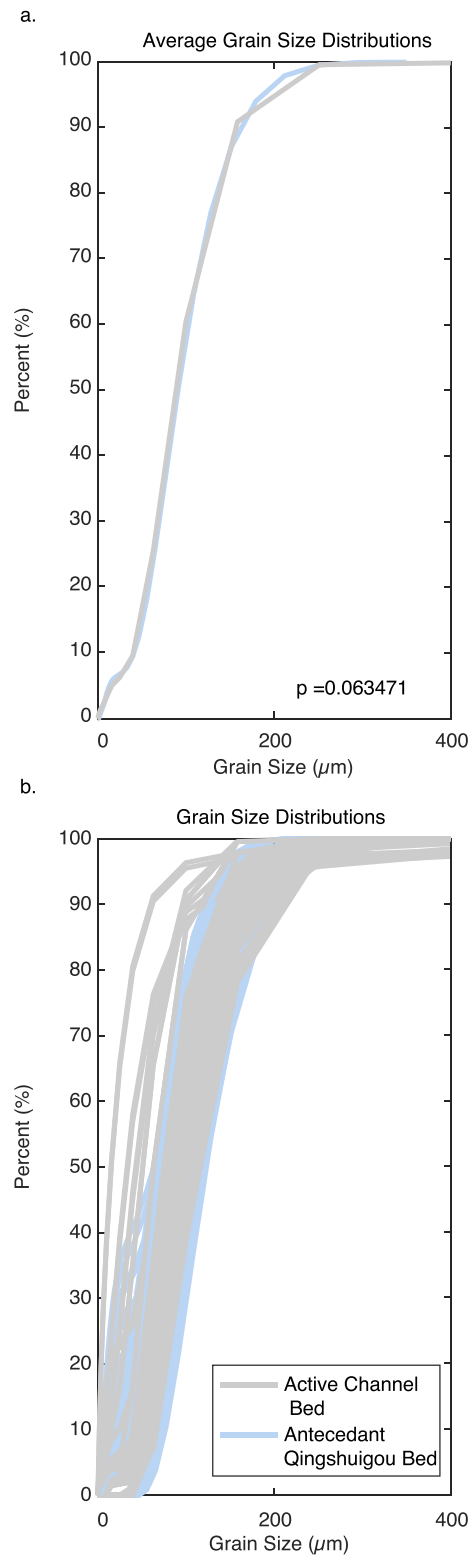


**Figure 5.** (a) Grain distributions from sand samples collected from cores, compared to samples collected from the active Huanghe channel bed, by using a two-sample Kolmogorov-Smirnov test. The result indicates that the average grain size distribution of the sandy sediment from the cores is indistinguishable from active Huanghe (with a 5% significance level). (b) A two-sample K-S test used to compare randomly chosen core samples to randomly chosen active Huanghe bed samples; for 69% of the tests, the two samples are from the same continuous distribution (with a 5% significance level).

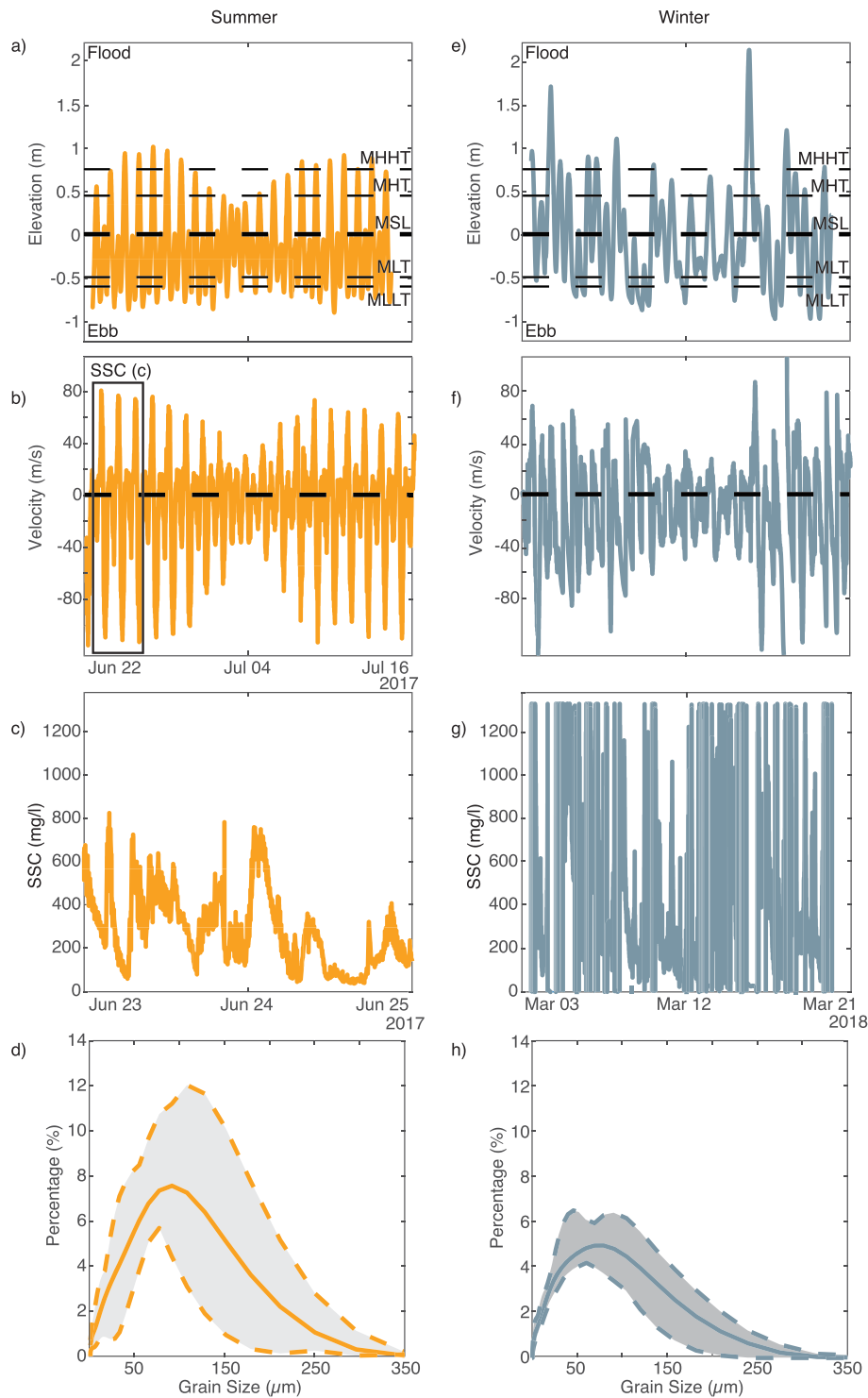


**Figure 6.** (a, e) Channel time series of water elevation, (b, f) near-bed velocity, (c, g) suspended-sediment concentration, and (d, h) grain size distributions of channel bed sediment with the solid line representing the mean of all samples, and the gray envelope bounded by dashed orange lines demarcates the maximum and minimum grain size sample distributions, with the average median grain size,  $D_{50}$ , noted. Note that a–d (orange) represent summer measurements, and e–h (blue) represent winter measurements. For both water depth and velocity in summer, the highest values are associated with spring tide. Suspended-sediment concentration for summer is only a 3-day period during spring tide, delineated by the black rectangle in (c). The largest values were measured at ebb tide (maximum concentration:  $\sim 700$  mg/L. Overall average median value is  $80 \mu\text{m}$ ). Winter storms (4, 8, and 14 March) have an important impact. High values ( $>1$  m/s) occur during winter storms. (g) Near-bottom SSC, measured during a winter 2018. Values exceeded the limits of the OBS ( $1,200$  mg/L), whereupon the instrument recorded “0” values. Overall average median value is  $60 \mu\text{m}$ .

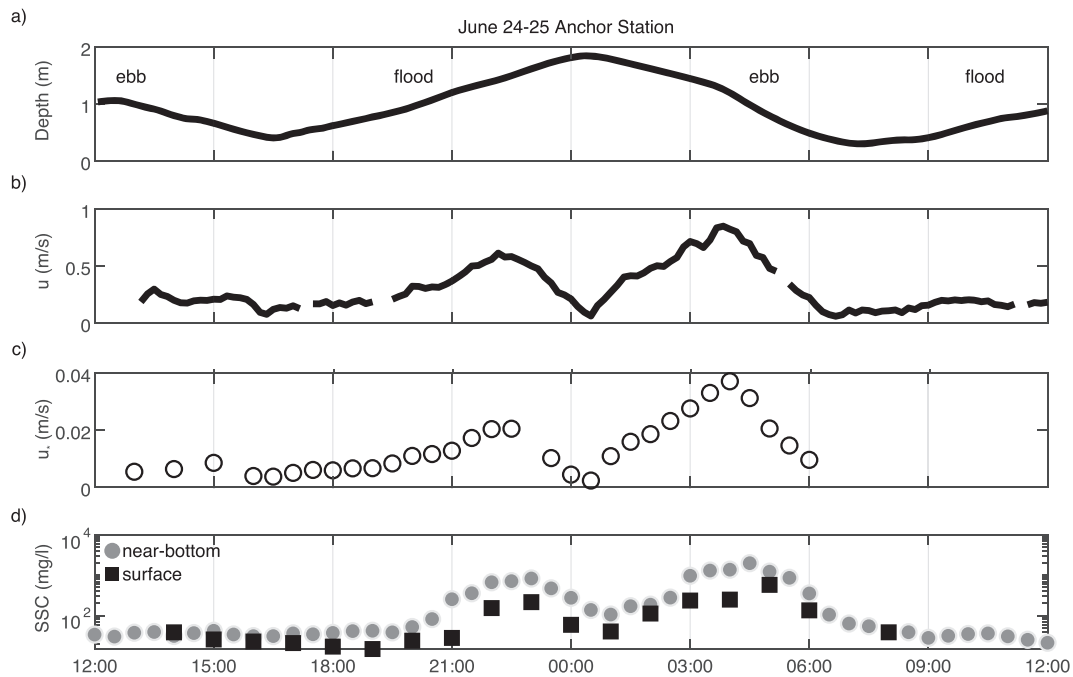


**Figure 7.** Data from over a 25-hr period when a measurement (anchor) station was conducted. (a) Channel water depth. (b) Depth-averaged velocity recorded by the ADCP, with the highest values during ebb flow. (c) Shear velocity,  $u_*$ , using a law-of-the-wall relationship applied to velocity profiles. (d) Near-bottom SSC measurements ( $2 \times 10^1$  to  $2 \times 10^3$  mg/L) and surface sediment concentration ( $1.5 \times 10^1$  to  $5.8 \times 10^2$  mg/L).

TCM located at T12 was fully inundated and recorded velocity up to 1 m/s. However, during the measurement station, the TCM was not submerged due to low water level, rendering the data unusable. Overall, SSC during the winter measurement station was relatively low compared to the summer

measurement station measurements. Near-bottom SSC measured during the measurement station was  $2.3 \times 10^1$  to  $4.7 \times 10^2$  mg/L. Surface SSC measurements range  $2.4 \times 10^1$  to  $4.2 \times 10^2$  mg/L. At all sample intervals, the SSC measurements are similar at the channel bed and surface. The median grain size of the bed samples collected during the winter measurement station ranges 31–50  $\mu\text{m}$  (Figure 6 h).

Measurements of water depth, velocity, and SSC during the winter measurement station do not reflect storm conditions and do not provide data for when sediment-laden water emerges onto the mudflat.

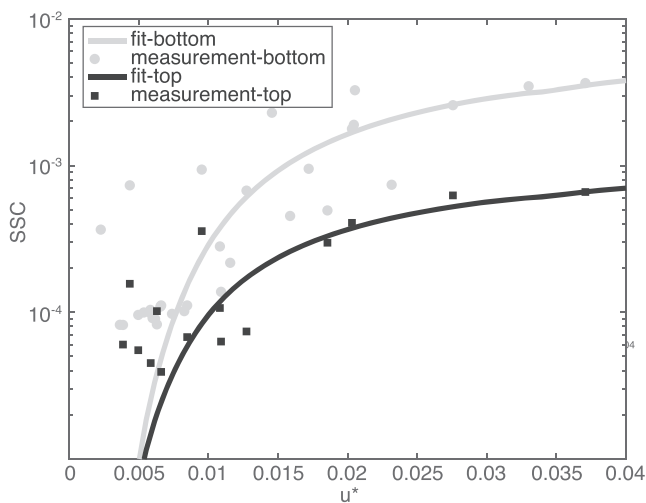


**Figure 8.** Suspended sediment concentration measurements collected near the tidal channel bed and surface, evaluated with respect to near-bed shear velocity (Figure 7). The data are fit using a Rouse formulation for suspended sediment concentration of bed material, where  $c_b$  and  $w_s$  are free parameters. The near-bottom SSC and  $u_*$  relationship have an  $R^2$  of 0.76, a predicted  $c_b$  value of 0.005 (SE = 0.001), and a predicted  $w_s$  of 0.002 m/s (SE =  $3.27 \times 10^{-4}$ ). The near-surface SSC and  $u_*$  relationship have an  $R^2$  of 0.83, a predicted  $c_b$  of  $5.72 \times 10^{-4}$  (SE =  $1.52 \times 10^{-4}$ ) and a predicted  $w_s$  of 0.002 (SE =  $3.11 \times 10^{-4}$ ).

#### 4.4. Mudflat Observations

During summer deployment, water inundated the mudflat during high tide for 4 days leading up to and following the spring tide (i.e., total of eight days of inundation). The maximum inundation was 0.5 m (Figure 7a). Following spring tide, the maximum daily water depth over the mudflat tapered until there was no inundation. The ADV located on the mudflat at T12, when sufficiently inundated, recorded velocity values that ranged from 0.01–0.20 m/s at 0.16 m above the mudflat (Figure 10a). The records indicate that the highest velocity occurs with the onset of flood tide and the waning of the ebb tide. During slack tide, velocity was as low as 0.01 m/s and lasted 480–1,400 s.

EAWM events observed during the winter survey amplified high tide so as to enhance water depth on the mudflat (Figure 10b). PT measurements recorded up to 1.20 m of water inundating the mudflat during

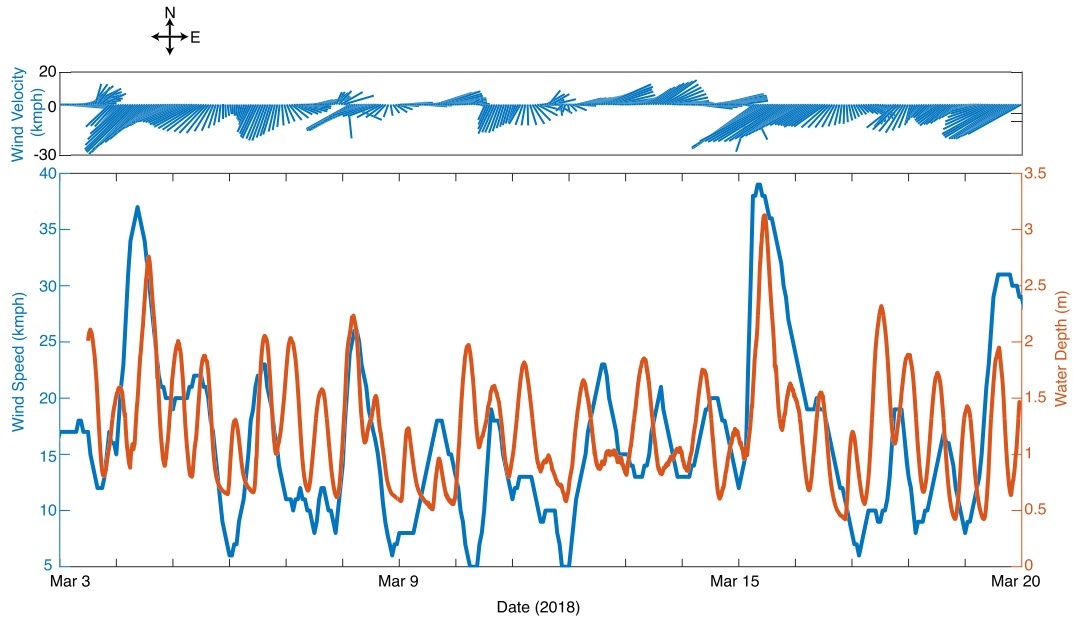


**Figure 9.** Wind velocity (top plot) and wind speed and tidal channel water depth (bottom plot), measured in the tidal channel at Transect 12 (Figures 2a and 2c) for the winter 2018 field survey. At the onset of winter storms, high wind velocity corresponds to a large water depth in the tidal channel. With the cessation of high wind velocity, water depth decreased (hourly wind data are sourced from World Weather Online for Dongying).

northeasterly wind events. However, with the cessation of high-velocity northeasterly winds, tides were suppressed so that high tide did not inundate the mudflat until >24 hr after the wind events ceased. Throughout the monitoring period, the ADV located on the mudflat at T12 recorded velocity values that ranged from 0.10–0.60 m/s at 0.16 m above the mudflat (Figure 10b).

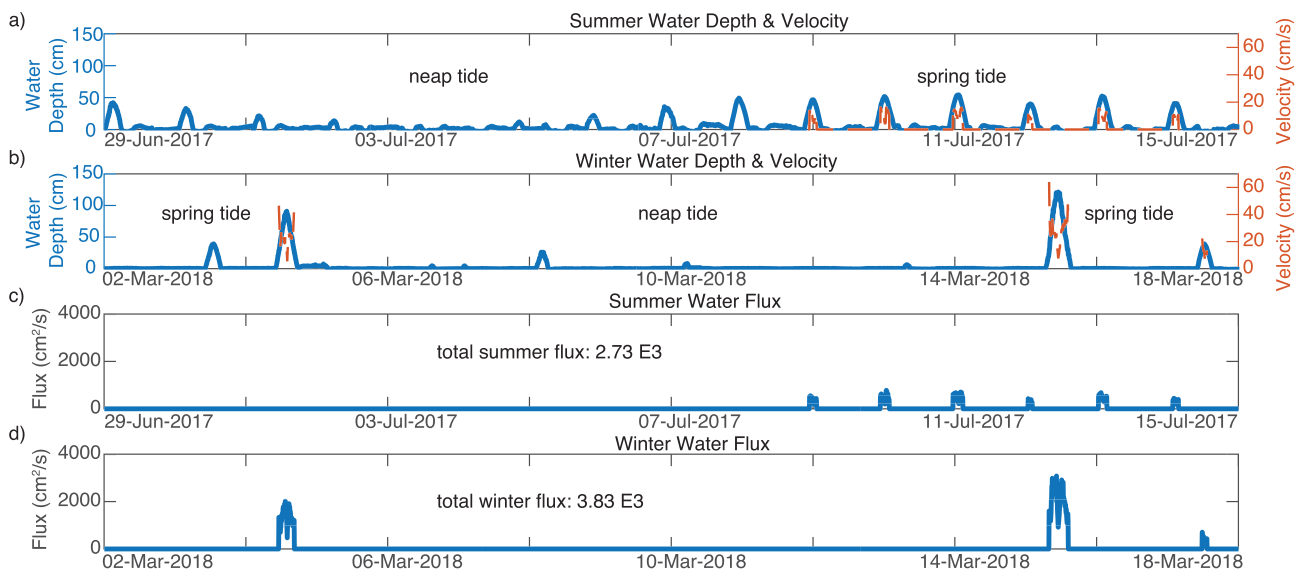


**Figure 10.** Current speed and water depth data collected from the mudflat during the summer 2017 and winter 2018 field campaigns, using instruments placed 150 m from the tidal channel bank, and a collocated ADV and pressure transducer (Figures 2a and 2c). Water depth (blue line, a–d) and current velocity (dashed red line, a–d) data were collected during (a) summer and (b) winter surveys. During summer, inundation patterns are dictated by astronomical spring/neap cycles, where the mudflat is inundated with up to 0.50 m of water during spring tide, while very little inundation occurs during neap. During winter, storms associated with the EAWM perturb the astronomical tidal cycle, where the greatest inundation of the mudflat occurs during periods of high sustained wind speed, rather than spring tide. The highest inundation of the mudflat corresponds to both spring tide and setup by strong northeasterly wind. Though the mudflat is inundated more frequently during the summer, the total water flux to the mudflat is 40% greater in the winter than during the summer ( $3.83 \times 10^3$  vs.  $2.73 \times 10^3$ , respectively).

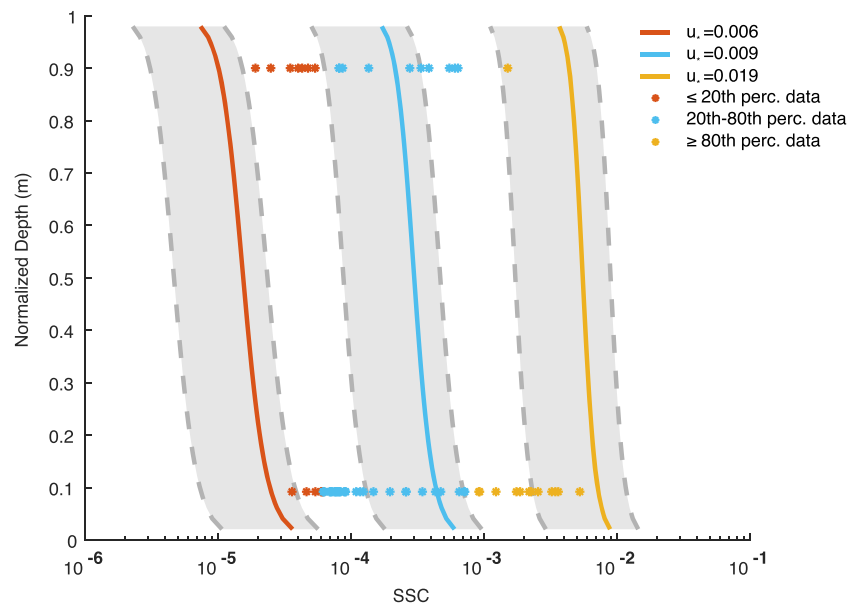


**Figure 11.** Bed material concentration profiles modeled using the 20th, 50th, and 80th percentile  $u_*$  values (solid red, blue, and yellow lines, respectively) plotted to depth normalized the maximum spring tide water depth for the summer 2017 measurement station at Transect 12 (Figure 7a). Solid lines are determined using the average grain size distribution measured on the tidal channel bed; the gray envelopes depict the range of predicted SSCs for measured grain size distributions produced from all samples ( $n = 7$ ). The measured near-bottom and surface SSC associated with the measured  $u_*$  value is displayed in like colors (i.e., red asterisks are measured SSC values for the 20th percentile  $u_*$  and below). The blue asterisks are measured SSC for all  $u_*$  values between the 20th and 80th percentiles. The yellow asterisks are measured SSC for all  $u_*$  values over the 80th percentile.

#### 4.5. SSC Model

High correlation between the local near-bed shear stress and measured SSC suggests that local resuspension is likely important for sediment concentration within the tidal channel (Figure 8). The measurement station conducted during summer 2017 provides a data set to constrain suspended-sediment profiles for conditions when water inundates the mudflat (equation (1)–(4), Figure 11). Using a shear stress value determined from near-bottom velocity profiles (Figure 7c), equation (1) predicts that over the range of measured flow conditions and sediment composition, the top 0.5 m of the water column maintains a volumetric SSC of  $5.1 \times 10^{-6}$  to  $6.2 \times 10^{-3}$ . Comparing predicted and measured values, SSC profiles encompass the range of measured near-bottom and surface SSC. For all SSC measurements, a wash load concentration value ( $2 \times 10^{-5}$ ) has been removed from the total concentration, as determined by SSC concentrations at the top of the water column during slack tide. This lower 20th percentile of SSC measurements overlaps the model for SSC using the 20th percentile  $u_*$ , and the upper 80th percentile SSC measurements overlap the model for SSC using the 80th percentile  $u_*$ . The SSC model generated with the 50th percentile  $u_*$  value is bounded by SSC measurements between the 20th and 80th percentiles (Figure 11). Notably, though the predicted SSC profiles do encompass the range of observed SSC, at low  $u_*$ , the predicted SSC profile only overlaps the lowest observation, while at high  $u_*$ , the predicted SSC profile only overlaps the highest observation. This suggests that while resuspension of tidal channel bed material can explain much of the observed SSC, it is likely that a mobile pool of fine sediment that is not incorporated into the bed material contributes to the observed sediment in suspension.

The model is applied for the 20th, 50th, and 80th percentiles measured  $u_*$  values and concomitant water depths. An important assumption is that sediment suspended to elevations higher than the adjacent mudflat surface is transported onto the mudflat. Using the measured range of slack tide duration (480–1,400 s and defined as velocity  $< 5$  cm/s; Renshun (1992)), sediment settles at each particle's settling velocity. The resulting grain size distribution of the deposit is compared to measurements. It is determined that the grain size distribution of particles settling during a slack tide duration of 400–600 s predicts the best match compared to measurements (Figure 12), which is in good agreement with observed slack duration (Figure 9). In this

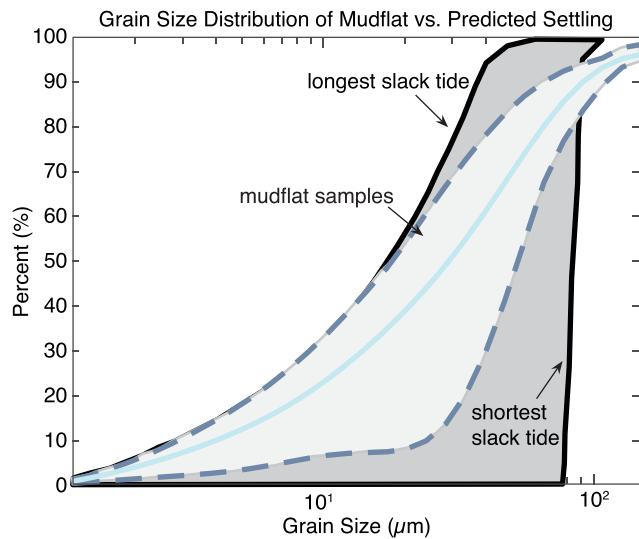


**Figure 12.** Grain size distributions of samples collected from the mudflat (locations shown in Figure 3a) as shown by the gray envelope, where the solid blue line denotes the average cumulative grain size distribution. The solid black lines are cumulative grain size distributions predicted to deposit for a time period of slack water, based on the sediment sizes for the top 0.5 m of the water column, calculated from a Rouse model for conditions measured during the summer 2017 field campaign. Note that the predicted grain size distributions are closest to the measured values for longer slack tide duration.

scape, could influence the potential to reoccupy abandoned channels as flow pathways upon future avulsions. Evaluating the processes that impact the morphology of abandoned channels and their associated lobes is therefore important to understand overall delta evolution. In this study, sedimentation patterns of the abandoned Qingshuigou deltaic distributary channel and its lobe are evaluated. This particular lobe is unique because its channel was completely cut off from an upstream input of sediment and water, so its evolution is dictated by marine and atmospheric processes. During low tide, water is contained in the tidal channel and the mudflat is exposed; conversely, at high tide, sediment-laden water inundates the mudflat (Figures 14a and 14b). Meanwhile, seasonal wave and wind patterns affect water elevation and sediment concentration along the channel and across the mudflat. Filling of the channel must be accomplished with marine-derived sediment due to its cutoff from the primary Huanghe. The magnitude and timing of sedimentation processes will be assessed using measurements of sediment and hydrodynamic properties. These data will then be used to validate a model for timing and magnitude of channel filling, which over time converts the abandoned channel into a mudflat.

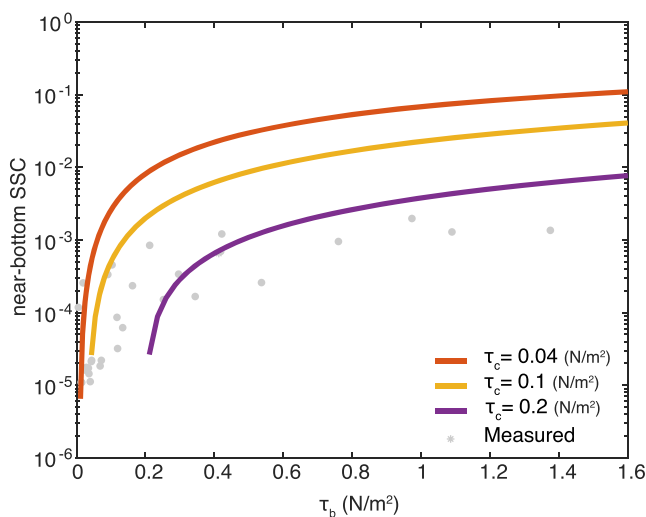


**Figure 13.** Near-bottom volumetric SSC, measured using the near-bottom water samples during the summer 2017 measurement station at Transect 12, plotted as a function of corresponding  $\tau_b$ . The near-bottom SSC predicted by equation (5) is shown as the solid lines for a range of  $\tau_c$ .

scenario, the finest sediment ( $<16 \mu\text{m}$ ) is treated as flocculated and maintains a  $w_s$  of 1 mm/s (Smith & Friedrichs, 2011).

The observed and modeled relationship between  $\tau_b$  and near-bottom SSC using different  $\tau_c$  is shown in Figure 13. At low  $\tau_b$  values, all predicted near-bottom SSCs are within the range of measured field values (gray circles); however, for all  $\tau_c$ , departure between model and measurement occurs with increasing  $\tau_b$ . SSC profiles in Figure 11 are generated using the lowest  $\tau_c$  value in Figure 13, because higher  $\tau_c$  values fail to entrain sediment at  $\tau_b$  values determined during the measurement station. However, it should be noted that the near-bottom SSC model does not match the shape of the observed near-bottom SSC measurements at any tested value of  $\tau_c$ . Furthermore, this value of  $\tau_c$  is an order of magnitude lower than values reported in modeling papers for cohesion in deltaic environments (Edmonds & Slingerland, 2009; Lanzoni & D'Alpaos, 2015), as well as field observations of the entrainment of consolidated cohesive material (Dunne et al., 2019). In environments with fine sediment,  $\tau_c$  is sensitive to the time duration over which consolidation can occur. For this system, where tides are mixed and semidiurnal, slack tide is typically less than 600 s and so there is little time for consolidation. This could be why relatively low values of  $\tau_c$  provide best model fits to observed near-bottom and surface SSC measurements (Figure 11).

## 5. Discussion

The extent of infilling of abandoned distributary channels, and the tendency for them to remain as topographic lows on a fluvial deltaic landscape, could influence the potential to reoccupy abandoned channels as flow pathways upon future avulsions. Evaluating the processes that impact the morphology of abandoned channels and their associated lobes is therefore important to understand overall delta evolution. In this study, sedimentation patterns of the abandoned Qingshuigou deltaic distributary channel and its lobe are evaluated. This particular lobe is unique because its channel was completely cut off from an upstream input of sediment and water, so its evolution is dictated by marine and atmospheric processes. During low tide, water is contained in the tidal channel and the mudflat is exposed; conversely, at high tide, sediment-laden water inundates the mudflat (Figures 14a and 14b). Meanwhile, seasonal wave and wind patterns affect water elevation and sediment concentration along the channel and across the mudflat. Filling of the channel must be accomplished with marine-derived sediment due to its cutoff from the primary Huanghe. The magnitude and timing of sedimentation processes will be assessed using measurements of sediment and hydrodynamic properties. These data will then be used to validate a model for timing and magnitude of channel filling, which over time converts the abandoned channel into a mudflat.

### 5.1. Sedimentation and Stratigraphy Patterns of the Qingshuigou Channel Fill

The shallow stratigraphy of the abandoned Qingshuigou channel demonstrates a grain size transition that is interpreted to reflect a change from sediment accumulating as part of the active river channel (fluvial origin) to mudflat sedimentation (marine origin). This assertion is bolstered by two-sample K-S tests that show that sediment grain size distributions of the sand from the lower portions of channel cores and that of the bed material found in the modern Huanghe are statistically indistinguishable (Figure 5). This implies that the sand is channel bed material deposited by the active river before abandonment. As such, due to the cutoff from the

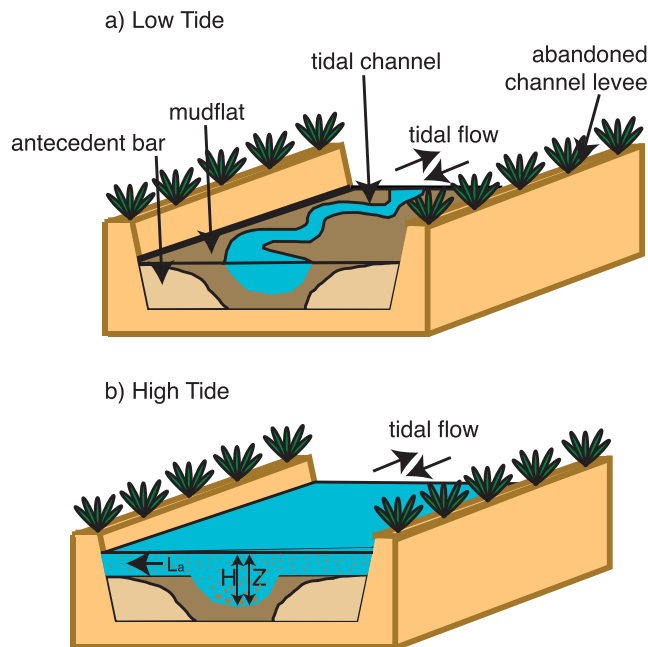


**Figure 14.** Illustration (not to scale) representing sediment infill of the Qingshuigou abandoned channel. Sediment-laden water is conveyed by a tidal channel. (a) During low tide water is contained within the tidal channel. (b) At high tide, sediment-laden water leaves the tidal channel and inundates the adjacent mudflat. SSC and grain size varies with elevation above the channel bed,  $Z$  (Figure 11, equation (1)). Sediment is transported onto the mudflat and deposited, traveling a distance described by  $L_{am}$  (see equation (8)). Sediment deposits atop the antecedent channel bed topography, creating spatially variable thickness of this material in the abandoned channel bed.

active fluvial channel, the mud deposited in the channel (i.e., overlying the sand) must be derived from a marine source.

The overlying mud that drapes the antecedent fluvial deposit ranges in thickness from approximately 0.1 to 1.78 m (Figure 4a and 4b). The grain size distribution of samples shows no spatial (vertical, horizontal) trends (Figures 4a and 4b). These observations are atypical of what is found for many tidal flats: As fluid velocity and shear stress diminish away from the tidal channel, sediment deposit thickness and grain size typically reflect this gradient and systematically thin and fine, respectively (Flemming, 2012; Friedrichs, 2011). Indeed, there seems to be no relation in terms of marine-derived sediment thickness and distance from the primary tidal channel (Figure 4b). Instead, we speculate that the fluvial channel topography was left to be inundated by water and sediment upon abandonment; in essence, the fluvial channel features were “frozen” in place upon avulsion and subsequently buried by marine sediment. To first order, it is expected that the distribution of mud thickness varies inversely to the elevation of the former channel topography. To test this supposition, Landsat imagery of the channel prior to abandonment was used to delineate the location of the channel thalweg and bars (Figure 15a).

Figures 15b and 15c show the interpreted thalweg and bars and core locations coded based on mud thickness (respectively). While it is not possible to know the exact elevations within the antecedent channel, the thalweg is inferred based on the location of water during a low discharge condition, while the bar tops are assessed based on the presence of the lighter buff color, interpreted to indicate relatively dry sediment (compared to the darker sediment adjacent to the water, which is interpreted to be saturated). Comparing locations within the antecedent thalweg and on the bar tops (Figure 15d), mud thickness over channel bars is on the scale of decimeters, and no greater than 0.65 m (Figure 15d), with a mean thickness of 0.18 m. For the core locations identified to have been collected in the former thalweg, maximum mud deposit thickness is much higher and approaches 1.8 m and averages 0.26 m.

This analysis indicates that the mud deposit is thicker over the antecedent thalweg and thins overtop former bars. This supports the hypothesis that spatial variability in mud thickness is conditioned by the underlying antecedent channel topography left behind after an avulsion, rather than variable accumulation rates based on proximity to the tidal channel. Still, the notion that marine-derived mud passively infills the channel features of the abandoned Qingshuigou channel is bolstered by understanding water and sediment exchange between the tidal channel and the adjacent mudflat. These assessments constrain sedimentation rates and therefore the timing of channel filling and conversion to a mudflat.

## 5.2. The Role of Resuspension of Tidal Channel Bed Sediment for Mudflat Aggradation

The seasonal variability in grain size composition of the active tidal channel bed reflects hydrodynamic processes both within and outside the channel (i.e., the Bohai Sea; Figure 6). Multiple lines of evidence indicate that the dominant signal of measured SSC is due to local resuspension of bed material by tidal currents in the channel. First, as discussed in sections 4.3.1 and 4.3.2, during summer months, SSC and  $u_*$  are correlated for both the lower and upper portions of the water column ( $R^2 = 0.76$  and  $0.83$ , respectively). As noted in section 4.5, the Rouse model predicts most, but not all, of the observed SSC; specifically, the Rouse model underpredicts and overpredicts at low and high  $u_*$  conditions, respectively (Figure 11). For the former case, it is speculated that this could indicate a mobile pool of near-bed fine sediment available to enhance SSC (Mathew & Winterwerp, 2017). This has been noted to arise in other systems during slack tide conditions, when fine sediment settles through water column and collects near the bed (Mathew & Winterwerp, 2017).

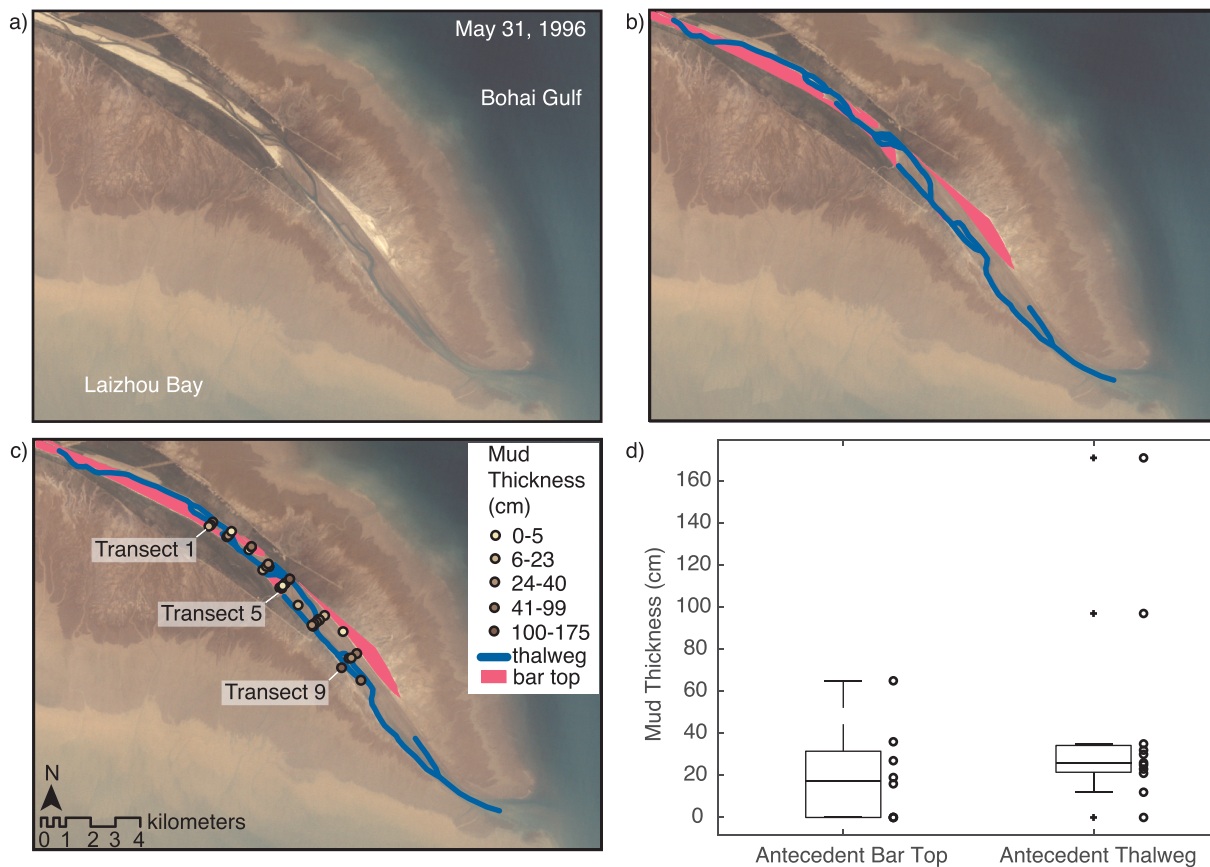


**Figure 15.** (a) Landsat 5 image of the Qingshuigou lobe acquired 31 May 1996, 1 month prior to avulsion. (b) The channel thalweg (blue line) is identified based on the occurrence of water. The lighter buff color in this image is assumed to be dry sediment part of the elevated channel bar top (pink). (c) Core and pit locations, with deposit thickness coded by color. (d) Boxplots of mud thickness for cores and pits located on former bar tops and within the former thalweg. The mean mud thickness on the bar tops is 0.18 m, while the mean thickness within the thalweg is 0.26 m. The total range of mud thickness on the bar tops is 0.65 m, while the range within the thalweg is up to 1.78 m.

Second, sediment size measured on the mudflat can be used to evaluate the characteristic distance over which grains are transported in suspension by tidal currents, using the advection length ( $L_{ao}$ ), computed as follows:

$$L_{ao} = U \frac{h}{w_s} \quad (6)$$

In a conservative case,  $U$  is the maximum measured tidal current speed (1 m/s),  $h$  is the maximum measured tidal channel water depth (2.5 m), and  $w_s$  is the settling velocity of the median grain size of sediment in transport (for mudflat sediment,  $32 \mu\text{m}$ , which possesses a  $w_s$  value of approximately 1 mm/s). The calculated  $L_{ao}$  is 2.5 km, which is about 50% shorter than the distance between the measurement site (T12) and the shoreline and a factor of 4 less than the total length of the tidal channel. This suggests that for much of the abandoned lobe, surface sediment on the mudflat was most recently resuspended and transported from the tidal channel before being deposited on the mudflat.

As noted above, the tidal channel fines during the winter, in particular, in association with EAWM events, when intense wave activity reworks relatively fine offshore deposits (Figure 6). It is believed that this produces elevated SSC at the seaward boundary, and landward directed transport of this material, facilitated by tides. As sediment concentration generated by waves offshore is higher than the local shear stress conditions in the tidal channel, material likely settles in the tidal channel, thereby fining the bed. During fair weather conditions, SSC is equilibrated to local hydrological conditions in the tidal channel (Figure 8), and fine material imported during the winter season is removed, resulting in coarsening of the bed.

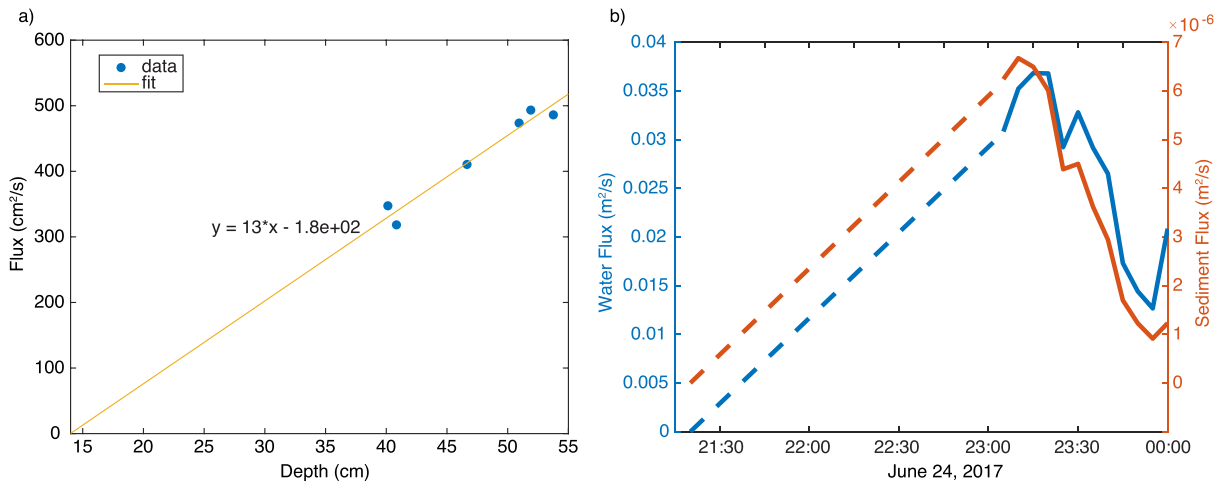


**Figure 16.** (a) Water flux as a function of depth of inundation, calculated based on velocity and depth data recorded on the mudflat by the ADV and pressure transducer, respectively. The relationship between depth ( $x$  axis) and water flux ( $y$  axis) is fit by a linear regression, and the function of this best fit is used to estimate water flux when the ADV head is not fully submerged. (b) Water flux (blue line) calculated for a spring flood tide over the mudflat on 24 June 2017 at point PT2 (Figure 2c) on Transect 12. Sediment flux (red line) is estimated for the same time and location as the product of the spring flood tide water flux and the concentration measured at the top of the water column during the measurement station.

Sediment suspended by tidal currents and transported to the adjacent mudflat settles from suspension during slack tide periods, whereby the predicted grain size of material in suspension matches the grain size of sediment samples collected from the mudflat (Figure 12, and more below, in section 5.3). Notably, during the measurement station, near-zero velocity conditions in the tidal channel coincide with a near-surface SSC of  $\sim 2 \times 10^{-5}$ . It is likely that the material remaining in suspension is too fine to settle over the duration of slack tide and thus does not deposit on the mudflat.

### 5.3. Field Measurements to Constrain Sedimentation in the Qingshuigou Channel

Tidal inundation of the Qingshuigou lobe channel varies seasonally. In fair weather (summer) months, flooding patterns are dominated by spring/neap and semidiurnal cycles, with  $\sim 0.5$  m of water covering the mudflat during high high spring tide (Figures 6a and 6b). During winter months, spring/neap cycles are disrupted by high storm surge water levels associated with episodic EAWM (Figure 6e and 6f). At the onset of a wind event, tidal fluctuations are enhanced by strong wind from the northeast, and high high spring tide inundates the flat with  $\sim 1.2$  m of water. However, following the initial high-water event, northeasterly wind speed decreases, which dampens tidal amplitude (Figure 9).

To evaluate the seasonal changes in water and sediment inundating the Qingshuigou mudflat, we calculate a width-averaged water flux ( $q_w$ ) (equation (7)) using ADV ( $u$ , m/s) and PT data ( $h$ , m/s):

$$q_w = u * h, \tag{7}$$

When the ADV is not fully submerged (i.e., water over the mudflat is  $< 0.36$  m),  $q_w$  is estimated using a linear regression function fit to the calculated values (Figure 16). The time-integrated water flux to the mudflat over a summer spring/neap cycle is  $0.27 \text{ m}^2/\text{s}$ , and for winter this value increases to  $0.38 \text{ m}^2/\text{s}$ .

Sediment flux to the mudflat is estimated as the product of  $q_w$  and sediment concentration of the surface water samples collected during the measurement station, when the adjacent mudflat was inundated. Hence, it is assumed that the near-surface SSC measurements from the channel represent SSC of water moving onto the adjacent mudflat (Mariotti & Fagherazzi, 2012). To calculate location and magnitude of sediment deposition, it is assumed that the suspended material settles through the water and deposits at a lateral distance from the tidal channel characterized by an advection length over the mudflat,  $L_{am}$  (Ganti, Lamb, & McElroy, 2014):

$$L_{am} = u \frac{h}{w_s}, \quad (8)$$

where  $h = 0.16$  m (the location above the mudflat where the ADV measures flow velocity),  $u$  is the measured flow velocity, and  $w_s$  is the settling velocity of the 50th percentile grain size of the sample population. All particles are presumed to deposit on the mudflat. The inundation intermittency is determined based on PT measurements that include several spring/neap cycles.

The volume of water transferred from the tidal channel to the mudflat during the summer (integrated over the time of the measurement station, 25 hr, which captures one diurnal tidal cycle) is  $186 \text{ m}^3$ . The sediment transferred to the mudflat ( $S_a$ ), based on measured concentration values, is  $0.03 \text{ m}^3$  (Figure 16b).  $L_{am}$  is calculated for the 10th, 50th, and 90th percentiles of the time-averaged measured flow velocities recorded during inundation (i.e., 0.03, 0.07, and 0.09 m/s, respectively). A total vertical aggradation,  $V_a$ , is calculated over the tidal cycle by

$$V_a = \frac{S_a}{L_{am}}. \quad (9)$$

Using the range of  $L_a$  values estimated, the resulting  $V_a$  outcomes over a diurnal tidal cycle are  $2.0\text{--}6.7 \times 10^{-3}$  m. Assuming a porosity of 30% (Morris & Johnson, 1967), a 70% annual inundation intermittency (based on field observation of the number of days the mudflat is inundated over a spring/neap cycle), and the range of  $L_a$  values (i.e., 10th, 50th, and 90th percentiles), the annual  $V_a$  values are 0.68, 0.95, and 2.22 cm, respectively. These values are inherently conservative because the calculation does not include winter observations for the basic reason that *in situ* measurements of SSC for surface water were not obtained when the mudflat was inundated, due to safety considerations. Nevertheless, other measurements of SSC collected during the winter field campaign show higher SSC than summer. Furthermore, there is greater inundation depth and longer inundation time over the mudflat during the winter relative to the summer conditions, particularly during storms; both conditions should produce enhanced mudflat sedimentation.

Notably, an equilibrium sediment transport model (i.e., Rouse model) is only used in the tidal channel where the spatial span is sufficiently long and nonequilibrium effects (e.g., scour lag and settling lag) are likely to be insignificant (An et al., 2018). However, because the mudflat has a much shorter spatial span, its modeling requires higher resolution. A nonequilibrium sediment transport model is implemented, whereby the advection length model is applied for the sediment deposition during flood tide, and the resuspension of sediment that settles onto the mudflat is close to zero during the subsequent ebb current. This may overestimate net accumulation of sediment (Postma, 1961; Ridderinkhof et al., 2000; Van Straaten & Kuenen, 1958).

In cores and pits, measured values of mud deposition range from decimeters to meters for over the past 20 yr (since abandonment), suggesting centimeter-scale annual rate of mud accumulation if the sedimentation rate is constant. Based on the previous analysis indicating thinner mud deposits over former fluvial bars and thicker mud deposits within the former thalweg (Figure 15), it is inferred that overall accumulation rates for the past 20 yr vary spatially as a consequence of the underlying fluvial topography. This is reasonable, considering that low points are preferentially inundated with sediment-laden water, and the elevation of bar tops, which possess very little mud cover, are intermittently inundated (i.e., only during spring high high tide). For example, considering the range of mud thickness values measured in the cores, assuming that this represents the totality of mud deposited since abandonment 20 yr ago, the average accumulation rate near the abandoned channel thalweg is  $1.3\text{--}8.9$  cm/yr, and the average accumulation rate for locations outside the thalweg is  $\sim 0.8$  cm/yr (Figure 15). This latter value, and the lower range of the former value, is consistent with the annual rates of sedimentation estimated in the advection-settling analyses presented above. These estimates are caveated in several ways, including seasonal variability in sediment delivery to the mudflat as a consequence of greater water inundation, and possibly greater sediment concentration, as measured during the energetic winter months, and the assumption that sediment delivered to the mudflat is deposited without bypass or subsequent removal.

Additionally, the grain size of sediment delivered to the mudflat may be predicted using a Rouse model (Lanzoni & D'Alpaos, 2015) informed by observations collected during the measurement station surveys within the adjacent tidal channel (Figure 12). The average grain size distribution predicted by the Rouse

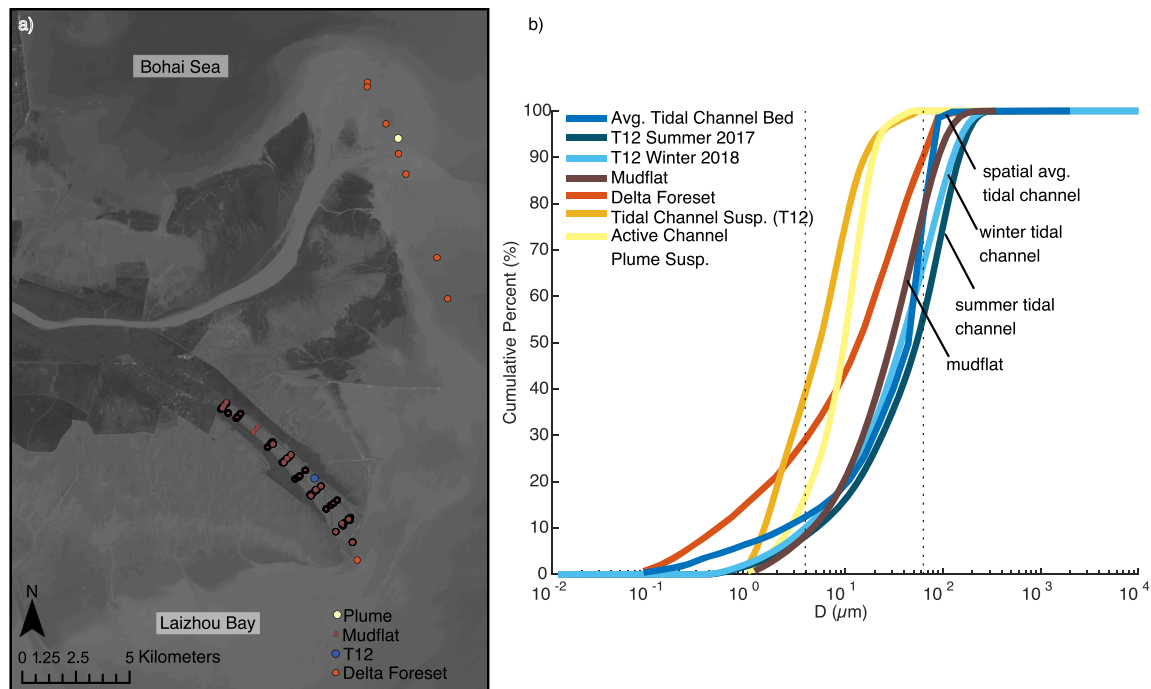


**Figure 17.** (a) Sample locations collected from within the tidal channel (Transect 12, blue circle), mudflat (brown circles), active channel plume (yellow circle), and subaqueous delta foreset (red circles). (b) The cumulative grain size distributions of sediment collected at locations in (a). The tidal channel bed (including winter, summer, and spatially averaged samples) most closely resembles mudflat distributions.

model for the upper 0.5 m of the tidal channel water column (i.e., that portion of the flow assumed to inundate the mudflat) is determined, whereupon it is assumed that all of this material deposit to the mudflat (note: particles finer than 16  $\mu\text{m}$  are assumed flocculated, and therefore possess a fixed settling velocity, as described above). This demonstrates that the calculated grain size distribution of sediment transferred to the mudflat is remarkably similar to the sediment measured on the mudflat (Figure 12).

Hence, both the rate of accumulation and grain size of sediment delivered from the tidal channel to the mudflat can be accounted for using basic models informed by observations collected from both the tidal channel and on the mudflat. Indeed, these assessments imply a sediment source derived locally, that is, the tidal channel, as the Rouse model estimates the concentration of *bed material* sediment (as opposed to washload, which is inherently finer).

#### 5.4. Constraining a Sediment Source for the Infilling of the Qingshuigou Lobe Channel

For nondeltaic fluvial channels abandoned by avulsion, channel infilling is facilitated by connectivity to the active channel and overbank sedimentation during floods. Abandoned deltaic distributary channels differ from their fluvial counterparts because the marine environment is an additional potential sediment source to fill the channel. For the Qingshuigou channel, the analyses presented above indicate that suspended sediment transported by the tidal channel provides material that fills the former channel, converting the lobe into an aggrading mudflat. The active Huanghe channel plume, and/or the shallow subaqueous region of the Huanghe delta foreset, could both be possible sources of material to the tidal channel. However, as a point of comparison, the grain size distributions of sediment collected from these environments compared to representative samples collected from the Qingshuigou mudflat (Figure 17) show that both the sediment from the plume and delta foreset are much finer than that of the mudflat.

The grain size distribution from the mudflat is most similar to the tidal channel bed, however there remains a seasonal contrast. For example, the median grain size values of the channel bed are 42–78  $\mu\text{m}$  for summer months (T12, Figure 6d), and 39–50  $\mu\text{m}$  during winter months (Figure 6h). The fining of the tidal channel bed during the winter season could be associated with the enhanced wave climate of the adjacent Bohai Sea as a consequence of the EAWM (Wang et al., 2014). The EAWM resuspends fine sediment from the delta

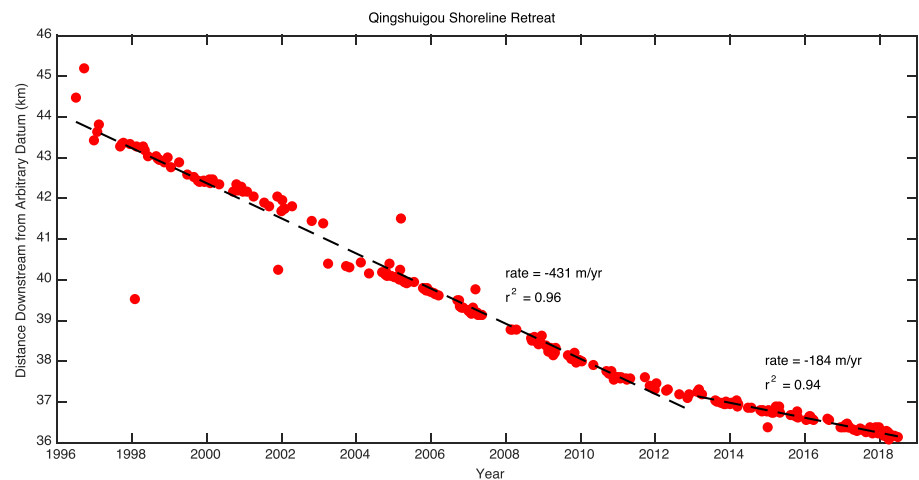


**Figure 18.** The Qingshuigou lobe distal shoreline position (1996–2018), extracted from satellite imagery, plotted as a distance from an inland datum. The shoreline retreated 431 m/yr from 1996–2012 and then slowed to 184 m/yr.

foreset, increasing sediment concentration in the adjacent marine environment (Wang et al., 2014). This sediment may move into the tidal channel, where it deposits. After the EAWM, wave energy is lower during quiescent summer months, and diurnal tidal currents rework the deposited sediment, suspending and transporting this material to the adjacent mudflat.

An additional factor to consider is that the Qingshuigou lobe is actively eroding, and therefore, its shoreline has receded since abandonment in 1996 (Bi et al., 2014; Zheng et al., 2017). In the 20 yr since, the shoreline retreated 7 km, with an average retreat rate of  $\sim 431$  m/yr between 1996 and 2013 and a retreat rate of  $\sim 184$  m/yr between 2013 and present (Figure 18). Wave energy, particularly during the winter months, is sufficient to remove and suspend sediment from the subaqueous portion of the lobe (Wang et al., 2010). This material is therefore readily transported via tidal currents into the abandoned Qingshuigou channel. Considering that the coastal system is eroding its own deltaic lobe sediment, this provides a source for the coarser material observed on the active mudflat, thereby accounting for the size fraction otherwise missing from the subaqueous foreset and active Huanghe plume.

### 5.5. Deltaic Channel Filling: To Completion or Not?

For abandoned distributary channels, channel dimensions are set by river discharge and the tidal prism (Bolla Pittaluga et al., 2015). The ability to fill a distributary channel with sediment sourced from the marine basin is set by the tidal range, specifically, the high high spring tide elevation, assuming that this is the elevation to where sediment may be deposited via water-borne transport. In areas where the tidal range is large, it is shown that filling of an abandoned channel could be extensive (Heath, 2009). An interesting case study comes from the Petitcodiac River in the Bay of Fundy (tidal range is  $\sim 7$  m), where in 1968 a causeway was constructed, cutting off water and sediment to the lower 55 km of the river. This resulted in sedimentation in the abandoned channel downstream of the causeway (via tidal transport of marine sediment) and annealing the channel, which reduced its width by  $\sim 90\%$  in 12 yr (i.e., from 1 km to 100 m, (Locke et al., 2003)). The thickness of the deposited sediment reached 8 m, consistent with the tidal range. For the abandoned Qingshuigou channel, microtidal conditions ( $\sim 1.5$  m) render tides incapable of reaching the elevation of the former channel levees, which presently extend up to 0.9 m above the high high tide elevation (Figure 2c). Hence, it is expected that abandoned channels of the Huanghe cannot be completely filled (if the channels maintain a self-similar levee height).

Beginning in 1931, channel relocation of the Huanghe on its delta occurred through engineered avulsions (Figure 1), most likely where a natural avulsion was pending (Ganti, Chu, et al., 2014). Interestingly, for many of these artificial diversions (seven out of eight), the abandoned channel pathways are still discernable in satellite images, particularly in proximity to the node (i.e., cutoff point) of the avulsion. However, for all of these cases, sediment and water input to the abandoned channel were essentially instantaneously cut off (as

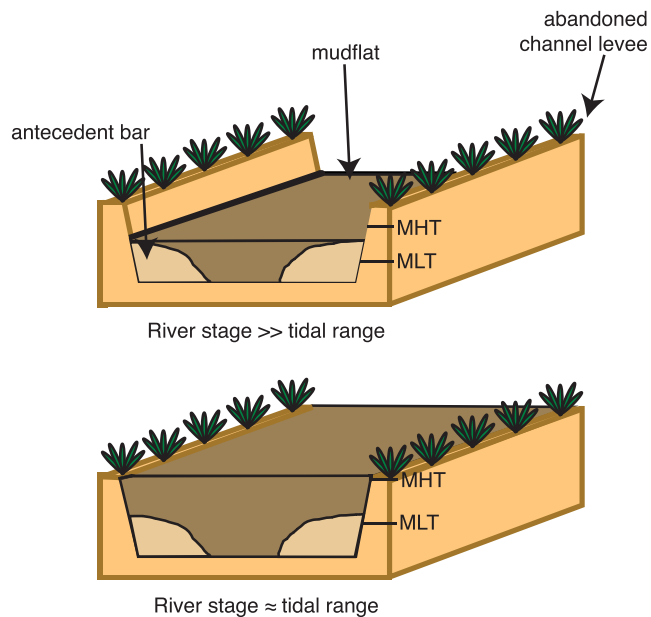


**Figure 19.** Illustration demonstrating abandoned channel fill potential in relation to the antecedent levee height. The channel bed and levee form when the channel is active. Upon abandonment, marine sediment, transported by tides, deposits in the channel and transforms the deposit into a mudflat. The degree to which the abandoned channel fills is a function of the tidal range (assuming water-borne transport of material) relative to the antecedent levee height. “MHT” and “MLT” indicate the mean high and low tide elevations, respectively. In (a), the levee height is higher than the tidal range, and so the abandoned channel cannot fully fill. In (b), the tidal range is large relative to the levee height and so it is possible to entirely fill the channel with sediment.

anneal the abandoned channel. To elucidate patterns of marine sediment filling of abandoned distributary channels, it is necessary to constrain the possible range of tidal inundation relative to the elevation of the levee height when the channel was active. Furthermore, as documented herein, patterns of deposit grain size and thickness may not be predictable when there is exclusively marine-sourced sediment. This is divergent from abandoned channels that maintain a connection to the active fluvial channel (Gray et al., 2016). In turn, these sedimentary signatures may prove useful for interpreting the rock record of ancient fluvial-deltaic systems.

## 6. Conclusions

Understanding the processes that lead to sediment infill of abandoned deltaic distributary channels has important implications for understanding delta dynamics, improving engineering practices, and interpreting the stratigraphic record. This study utilizes a modern example of the abandoned Qingshuigou distributary channel of the Huanghe, which was abandoned in 1996 via engineered avulsion, and has been subsequently filling with marine sediment delivered by tides. The shallow stratigraphy of the abandoned channel displays a transition from the formerly active channel to tidally delivered sediment. Observations of hydrodynamic conditions and sediment delivery within the abandoned channel confirm modern sediment accumulation.

On average, 0.50 m of mud has been deposited over the antecedent Qingshuigou fluvial channel bed. Stratigraphic observations, sediment flux monitoring, and modeling efforts indicate that modern accumulation rates on the mudflat are up to several centimeters per year. Field observations of mud thickness were explored for spatial trends; however, no trends exist as a function of distance from the tidal channel bank or with distance from the shoreline. Instead, the antecedent topography of the Huanghe channel bed exerts a primary control on mud deposit thickness.

in the situation of the Qingshuigou channel). For natural avulsions (prior to 1931), it is not possible to identify abandoned channel bodies and, as demonstrated in Figure 1, these historical natural avulsions on the Huanghe delta tended to traverse new pathways, rather than reoccupy former channels (Van Gelder et al., 1994). It is therefore proposed that natural deltaic avulsions, with the capacity to maintain a connection to the primary channel, fill from both the upstream and downstream directions, as influenced by fluvial and marine processes, respectively. This, in turn, creates favorable conditions for complete sediment filling of the abandoned channel and therefore limits the potential for reoccupation of former channels upon future avulsions. On the other hand, artificial avulsions are only capable of filling from the downstream direction and are thus limited in terms of filling by the upstream limit of tidal influence. Hence, it is expected that the remaining portion of these antecedent channels persists as topographic lows on the delta.

The lessons provided by the Huanghe delta indicate several important points. Under natural conditions, sediment delivery to an abandoned deltaic channel can arise from upstream (fluvial) and downstream (marine) sources. For the latter, the tidal range, relative to the levee height, determines the degree to which the channel may fill. The elevation of fluvial channel levees is, to first order, dependent on river stage during floods (Smith & Pérez-Arlucea, 2008), which for fluvially dominated deltaic channels is set primarily by water surface slope (Nittrouer et al., 2012). If the tidal range is low compared to the levee height (as in the case of the Qingshuigou lobe), then channels remain underfilled and topographic lows (Figure 19a). Alternatively, it is possible to fill abandoned channels if levee heights are comparable to the tidal range (Figure 19b). For the upstream (fluvial) situation, water and sediment input via connection to the main channel could work to fill the channel from upstream, which, when combined with downstream marine sediment, may work to fully

The sediment that comprises the tidal channel bed varies seasonally. Sediment that is suspended in the Bohai Sea during EAWM wave activity fines the tidal channel bed, where, throughout the remainder of the year, tidal currents rework and coarsen this material and transfer sediment onto the mudflat. The grain size distribution of material present on the mudflat can be attributed to bed material of the tidal channel, and so sediment is assumed to be supplied locally (i.e., from the tidal channel as opposed to directly from input from offshore).

The sedimentological record produced by infilling abandoned distributary channels provides insight for delta dynamics and the role of marine sediment delivery to nearshore environments. The degree of infilling and spatial characteristics of sediment infill are indicative of marine versus fluvial mechanisms for filling. The abandoned Qingshuigou levees exceed the elevation of the high high spring tide, so sediment sourced from the receiving basin is likely insufficient to fully anneal the channel.

### Acknowledgments

This study was supported by the National Science Foundation (NSF) EAR-1427262 and EAR-1427259, “Coastal SEES Collaborative Research: Morphologic, Socioeconomic, and Engineering Sustainability of Massively Anthropogenic Coastal Deltas: The Compelling Case of the Huanghe Delta.” We would like to thank the Hydrological Survey Bureau of the Yellow River Mouth and the Yellow River Institute of Hydraulic Research for facilitating the logistics of this fieldwork. We also gratefully acknowledge field support from Tian Dong, Chenliang Wu, Eric Barefoot, Michelle Mullane, Katie Lavallo, Liang Chen, Michael Lamb, and Gary Parker. The authors thank the efforts of three reviewers, including Giulio Mariotti and two anonymous reviewers. All code and data used for analyses and conclusions can be obtained online ([https://github.com/brandeeeee/publication\\_data/Channel\\_infilling\\_Huanghe](https://github.com/brandeeeee/publication_data/Channel_infilling_Huanghe)).

### References

- Aalto, R., Lauer, J. W., & Dietrich, W. E. (2008). Spatial and temporal dynamics of sediment accumulation and exchange along Strickland River floodplains (Papua New Guinea) over decadal-to-centennial timescales. *Journal of Geophysical Research*, *113*, F01S04. <https://doi.org/10.1029/2006JF000627>
- An, C., Moodie, A. J., Ma, H., Fu, X., Zhang, Y., Naito, K., & Parker, G. (2018). Morphodynamic model of the lower Yellow River: Flux or entrainment form for sediment mass conservation? *Earth Surface Dynamics*, *6*, 989–1010. <https://doi.org/10.5194/esurf-6-989-2018>
- Aslan, A., & Autin, W. J. (1999). Evolution of the Holocene Mississippi River floodplain, Ferriday, Louisiana: Insights on the origin of fine-grained floodplains. *Journal of Sedimentary Research*, *69*(4).
- Bi, N., Wang, H., & Yang, Z. (2014). Recent changes in the erosion-accretion patterns of the active Huanghe (Yellow River) delta lobe caused by human activities. *Continental Shelf Research*, *90*, 70–78. <https://doi.org/10.1016/j.csr.2014.02.014>
- Bolla Pittaluga, M., Tambroni, N., Canestrelli, A., Slingerland, R., Lanzoni, S., & Seminara, G. (2015). Where river and tide meet: The morphodynamic equilibrium of alluvial estuaries. *Journal of Geophysical Research: Earth Surface*, *120*, 75–94. <https://doi.org/10.1002/2014JF003233>
- Chamberlin, E. P., & Hajek, E. A. (2015). Interpreting Paleo-avulsion dynamics from multistory sand bodies. *Journal of Sedimentary Research*, *85*(2), 82–94. <https://doi.org/10.2110/jsr.2015.09>
- Chu, Z. X., Sun, X. G., Zhai, S. K., & Xu, K. H. (2006). Changing pattern of accretion/erosion of the modern Yellow River (Huanghe) subaerial delta, China: Based on remote sensing images. *Marine Geology*, *227*(1–2), 13–30. <https://doi.org/10.1016/j.margeo.2005.11.013>
- Dai, Z., Fagherazzi, S., Mei, X., Chen, J., & Meng, Y. (2016). Linking the infilling of the North Branch in the Changjiang (Yangtze) estuary to anthropogenic activities from 1958 to 2013. *Marine Geology*, *379*, 1–12. <https://doi.org/10.1016/j.margeo.2016.05.006>
- Dietrich, W. E. (1982). Settling velocity of natural particles. *Water Resources Research*, *18*(6), 1615–1626. <https://doi.org/10.1029/WR018i006p01615>
- Dunne, K. B. J., Jerolmack, D. J., Science, E., & Mechanics, A. (2019). Rivers shaped by the most erosion resistant material. 1–7.
- Edmonds, D. A., & Slingerland, R. L. (2009). Significant effect of sediment cohesion on delta morphology. *Nature Geoscience*, *105*–109. <https://doi.org/10.1038/NCEO730>
- Elgar, S., Raubenheimer, B., & Guza, R. T. (2005). Quality control of acoustic Doppler velocimeter data in the surfzone. *Measurement Science and Technology*, *16*, 1889–1893. Retrieved from <http://www.whoie.edu/science/AOPE/dept/Publications/093.pdf>
- Fitts, C. (2002). Groundwater Science (1st ed.). Retrieved from [https://books.google.com/books?id=AJPL3Z2k2hQC&pg=PA87&lpg=PA87&dq=assuming+a+water+density+of+1.025+g/cm3&source=bl&ots=MP40Z-aOEY&sig=UN63HuijiiYsaTBdyMjDINiXCE&hl=en&sa=X&ved=2ahUKEWjInODloq\\_fAhUCa60KHb5VBXUQ6AEwBHoECAUQAQ#v=one-page&q=assumingaw](https://books.google.com/books?id=AJPL3Z2k2hQC&pg=PA87&lpg=PA87&dq=assuming+a+water+density+of+1.025+g/cm3&source=bl&ots=MP40Z-aOEY&sig=UN63HuijiiYsaTBdyMjDINiXCE&hl=en&sa=X&ved=2ahUKEWjInODloq_fAhUCa60KHb5VBXUQ6AEwBHoECAUQAQ#v=one-page&q=assumingaw)
- Flemming, B. W. (2012). Siliciclastic back-barrier tidal flats. In *In Principles of Tidal Sedimentology* (pp. 231–267). Dordrecht: Springer. [https://doi.org/10.1007/978-94-007-0123-6\\_10](https://doi.org/10.1007/978-94-007-0123-6_10)
- Friedrichs, C. T. (2011). Tidal flat morphodynamics: A synthesis. In *In Treatise on Estuarine and Coastal Science* (Vol. 3, pp. 137–170). Waltham: Academic Press. <https://doi.org/10.1016/B978-0-12-374711-2.00307-7>
- Galloway, W. E. (1975). In M. Broussard (Ed.), *Process framework for describing the morphologic and stratigraphic evolution of deltaic depositional systems* (pp. 87–98). Houston, TX: Houston Geol Soc. Retrieved from [http://archives.datapages.com/data/hgssp/data/022/022001/87\\_hgs0220087.htm](http://archives.datapages.com/data/hgssp/data/022/022001/87_hgs0220087.htm)
- Ganti, V., Chu, Z., Lamb, M. P., Nittrouer, J. A., & Parker, G. (2014). Testing morphodynamic controls on the location and frequency of river avulsions on fans versus deltas: Huanghe (Yellow River), China. *Geophysical Research Letters*, *41*, 7882–7890. <https://doi.org/10.1002/2014GL061918>
- Ganti, V., Lamb, M. P., & McElroy, B. (2014). Quantitative bounds on morphodynamics and implications for reading the sedimentary record. *Nature Communications*, *5*(1), 1–7. <https://doi.org/10.1038/ncomms4298>
- Garcia, M. (2008). *Sedimentation Engineering* (M. Garcia, Ed.). Reston: American Society of Civil Engineers. <https://doi.org/10.1061/9780784408148>
- Gray, A. B., Pasternack, G. B., Watson, E. B., & Goñi, M. A. (2016). Abandoned channel fill sequences in the tidal estuary of a small mountainous, dry-summer river. *Sedimentology*, *63*(1), 176–206. <https://doi.org/10.1111/sed.12223>
- Hajek, E. A., & Wolinsky, M. A. (2012). Simplified process modeling of river avulsion and alluvial architecture: Connecting models and field data. *Sedimentary Geology*, *257*–260, 1–30. <https://doi.org/10.1016/J.SEDGEO.2011.09.005>
- He, L. (2019). Estimation of bankfull discharge in the lower Yellow River. *Water Resources*, *46*(2), 160–171. <https://doi.org/10.1134/S009780781902009X>
- Heath, K. M. (2009). *Fluid mud formation in the Petitcodiac River, New Brunswick*. Canada: Boston College.
- Hoitink, A. J. F., Hoekstra, P., & van Maren, D. S. (2003). Flow asymmetry associated with astronomical tides: Implications for the residual transport of sediment. *Journal of Geophysical Research*, *108*(C10), 3315. <https://doi.org/10.1029/2002JC001539>

- Kim, W., Mohrig, D., Twilley, R., Paola, C., & Parker, G. (2009). Is it feasible to build new land in the Mississippi River delta? *Eos, Transactions of the American Geophysical Union*, 90(42), 373–374. <https://doi.org/10.1029/2009EO420001>
- Lanzoni, S., & D'Alpaos, A. (2015). On funneling of tidal channels. *Journal of Geophysical Research: Earth Surface*, 120, 433–452. <https://doi.org/10.1002/2014JF003203>
- Le Hir, P., Roberts, W., Cazaillet, O., Christie, M., Bassoullet, P., & Bacher, C. (2000). Characterization of intertidal flat hydrodynamics. *Continental Shelf Research*, 20(12–13), 1433–1459. [https://doi.org/10.1016/S0278-4343\(00\)00031-5](https://doi.org/10.1016/S0278-4343(00)00031-5)
- Locke, A., Hanson, J. M., Klassen, G. J., Richardson, S. M., & Aube, C. I. (2003). The damming of the Petitcodiac River: Species, populations, and habitats lost. *Northeastern Naturalist*, 10(1), 39. <https://doi.org/10.2307/3858671>
- Ma, H., Nittrouer, J. A., Naito, K., Fu, X., Zhang, Y., Moodie, A. J., et al. (2017). The exceptional sediment load of fine-grained dispersal systems: Example of the Yellow River, China. *Science Advances*, 3(5), e1603114. <https://doi.org/10.1126/sciadv.1603114>
- Ma, H., Nittrouer, J. A., Wu, B., Lamb, M. P., Zhang, Y., Mohrig, D., ... Parker, G. (2019). Universal relation with regime transition for sediment transport in fine-grained rivers. *Proceedings of the National Academy of Sciences*, 1–6. <https://doi.org/10.1073/pnas.1911225116>
- Mackey, S. D., & Bridge, J. S. (1995). Three-dimensional model of alluvial stratigraphy: Theory and application. *Journal of Sedimentary Research*, 65(1).
- Mariotti, G., & Fagherazzi, S. (2011). Asymmetric fluxes of water and sediments in a mesotidal mudflat channel. *Continental Shelf Research*, 31(1), 23–36. <https://doi.org/10.1016/j.csr.2010.10.014>
- Mariotti, G., & Fagherazzi, S. (2012). Channels-tidal flat sediment exchange: The channel spillover mechanism. *Journal of Geophysical Research*, 117. <https://doi.org/10.1029/2011JC007378>
- Mathew, R., & Winterwerp, J. C. (2017). Surficial sediment erodibility from time-series measurements of suspended sediment concentrations: Development and validation. *Ocean Dynamics*, 67(6), 691–712. <https://doi.org/10.1007/s10236-017-1055-2>
- McLean, S. R. (1992). On the calculation of suspended load for noncohesive sediments. *Journal of Geophysical Research*, 97(C4), 5759. <https://doi.org/10.1029/91JC02933>
- Mohrig, D., Heller, P. L., Paola, C., & Lyons, W. J. (2000). Interpreting avulsion process from ancient alluvial sequences: Guadalope-Matarranya system (northern Spain) and Wasatch Formation (western Colorado). *GSA Bulletin*, 112(3), 1787–1803.
- Moodie, A. J., Nittrouer, J. A., Ma, H., Carlson, B. N., Chadwick, A. J., Lamb, M. P., & Parker, G. (2019). Modeling deltaic lobe-building cycles and channel avulsions for the Yellow River delta, China. *Journal of Geophysical Research: Earth Surface*, 2019JF005220. <https://doi.org/10.1029/2019JF005220>
- Morris, D. A., & Johnson, A. I. (1967). Summary of hydrologic and physical properties of rock and soil materials, as analyzed by the hydrologic laboratory of the U.S. Geological Survey. *Water Supply Paper*. Retrieved from, 1948–1960. <https://pubs.er.usgs.gov/publication/wsp1839D>
- Nienhuis, J. H., Ashton, A. D., Roos, P. C., Hulscher, S. J. M. H., & Giosan, L. (2013). Wave reworking of abandoned deltas. *Geophysical Research Letters*, 40, 5899–5903. <https://doi.org/10.1002/2013GL058231>
- Nittrouer, J. A., Shaw, J., Lamb, M. P., & Mohrig, D. (2012). Spatial and temporal trends for water-flow velocity and bed-material sediment transport in the lower Mississippi River. *Geological Society of America Bulletin*, 124(3–4), 400–414. <https://doi.org/10.1130/B30497.1>
- Pang, J., & Si, S. (1979). The estuary changes of the Huanghe River I. Changes in modern time. *Oceanologia Et Limnologia Sinica*, 10(2), 136–141.
- Postma, H. (1961). Transport and accumulation of suspended matter in the Dutch Wadden Sea. *Netherlands Journal of Sea Research*, 1. [https://doi.org/10.1016/0077-7579\(61\)90004-7](https://doi.org/10.1016/0077-7579(61)90004-7)
- Rahman, A. F., Dragoni, D., & El-Masri, B. (2011). Response of the Sundarbans coastline to sea level rise and decreased sediment flow: A remote sensing assessment. *Remote Sensing of Environment*, 115(12), 3121–3128. <https://doi.org/10.1016/j.rse.2011.06.019>
- Reitz, M. D., Jerolmack, D. J., & Swenson, J. B. (2010). Flooding and flow path selection on alluvial fans and deltas. *Geophysical Research Letters*, 37, L06401. <https://doi.org/10.1029/2009GL041985>
- Renshun, Z. (1992). Suspended sediment transport processes on tidal mud flat in Jiangsu Province, China. *Estuarine, Coastal and Shelf Science*, 35(3), 225–233. [https://doi.org/10.1016/S0272-7714\(05\)80045-9](https://doi.org/10.1016/S0272-7714(05)80045-9)
- Ridderinkhof, H., van der Ham, R., & van der Lee, W. (2000). Temporal variations in concentration and transport of suspended sediments in a channel-flat system in the Ems-Dollard estuary. *Continental Shelf Research*, 20(12), 1479–1493. [https://doi.org/10.1016/S0278-4343\(00\)00033-9](https://doi.org/10.1016/S0278-4343(00)00033-9)
- Roberts, H. (1997). Dynamic changes of the Holocene Mississippi River delta cycle. *Journal of Coastal Research*, 13(3), 605–627. Retrieved from <http://journals.fcla.edu/jcr/article/view/80176/77431>
- Rouse, H. B. (1937). Modern conceptions of the mechanics or fluid turbulence. Retrieved from <https://www.semanticscholar.org/paper/Modern-Conceptions-of-the-Mechanics-or-Fluid-Rouse/cc8798f6cb60da90468ffec7f93f182b95a1ebd9>
- Rowland, J. C., Lepper, K., Dietrich, W. E., Wilson, C. J., & Sheldon, R. (2005). Tie channel sedimentation rates, oxbow formation age and channel migration rate from optically stimulated luminescence (OSL) analysis of floodplain deposits. *Earth Surface Processes and Landforms*, 30(9), 1161–1179. <https://doi.org/10.1002/esp.1268>
- Saito, Y., Wei, H., Zhou, Y., Nishimura, A., Sato, Y., & Yokota, S. (2000). Delta progradation and chenier formation in the Huanghe (Yellow River) delta, China. *Journal of Asian Earth Sciences*, 18(4), 489–497. [https://doi.org/10.1016/S1367-9120\(99\)00080-2](https://doi.org/10.1016/S1367-9120(99)00080-2)
- Shi, B., Cooper, J. R., Pratalongo, P. D., Gao, S., Bouma, T. J., Li, G., et al. (2017). Erosion and accretion on a mudflat: The importance of very shallow-water effects. *Journal of Geophysical Research: Oceans*, 122, 9476–9499. <https://doi.org/10.1002/2016JC012316>
- Slingerland, R., & Smith, N. D. (2004). River avulsions and their deposits. *Annual Review of Earth and Planetary Sciences*, 32, 257–285. <https://doi.org/10.1146/annurev.earth.32.101802.120201>
- Smith, N. D., Cross, T. A., Dufficy, J. P., & Clough, S. R. (1989). Anatomy of an avulsion. *Sedimentology*, 36(1), 1–23. <https://doi.org/10.1111/j.1365-3091.1989.tb00817.x>
- Smith, N. D., & Pérez-Arlucea, M. (2008). Natural levee deposition during the 2005 flood of the Saskatchewan River. *Geomorphology*, 101(4), 583–594. <https://doi.org/10.1016/J.GEOMORPH.2008.02.009>
- Smith, S. J., & Friedrichs, C. T. (2011). Size and settling velocities of cohesive flocs and suspended sediment aggregates in a trailing suction hopper dredge plume. *Continental Shelf Research*, 31, S50–S63. <https://doi.org/10.1016/j.csr.2010.04.002>
- Sternberg, R. W., Kineke, G. C., & Johnson, R. (1991). An instrument system for profiling suspended sediment, fluid, and flow conditions in shallow marine environments. *Continental Shelf Research*, 11(2), 109–122. [https://doi.org/10.1016/0278-4343\(91\)90057-D](https://doi.org/10.1016/0278-4343(91)90057-D)
- Tamura, T., Saito, Y., Lap Nguyen, V., Oanh Ta, T. K., Bateman, M. D., Matsumoto, D., & Yamashita, S. (2012). Origin and evolution of interdistributary delta plains: Insights from Mekong River Delta. *Geology*, 40(4), 303–306. <https://doi.org/10.1130/G32717.1>
- Toonen, W. H. J., Kleinhans, M. G., & Cohen, K. M. (2012). Sedimentary architecture of abandoned channel fills. *Earth Surface Processes and Landforms*, 37(4), 459–472. <https://doi.org/10.1002/esp.3189>

- Van Gelder, A., Van Den Berg, J. H., Cheng, G., & Xue, C. (1994). Overbank and channelfill deposits of the modern Yellow River delta. *Sedimentary Geology*, *90*, 293–305. [https://doi.org/10.1016/0037-0738\(94\)90044-2](https://doi.org/10.1016/0037-0738(94)90044-2)
- Van Maren, D. S., & Winterwerp, J. C. (2013). The role of flow asymmetry and mud properties on tidal flat sedimentation. *Continental Shelf Research*, *60*, S71–S84. <https://doi.org/10.1016/j.csr.2012.07.010>
- Van Maren, D. S., Winterwerp, J. C., Wang, Z. Y., & Pu, Q. (2009). Suspended sediment dynamics and morphodynamics in the Yellow River, China. *Sedimentology*, *56*(3), 785–806. <https://doi.org/10.1111/j.1365-3091.2008.00997.x>
- Van Straaten, L. M. J. U., & Kuenen, P. H. (1958). Tidal action as a cause of clay accumulation. *SEPM Journal of Sedimentary Research*, *Vol.*, *28*. <https://doi.org/10.1306/74d70826-2b21-11d7-8648000102c1865d>
- Wang, H., Bi, N., Wang, Y., Saito, Y., & Yang, Z. (2010). Tide-modulated hyperpycnal flows off the Huanghe (Yellow River) mouth, China. *Earth Surface Processes and Landforms*, *35*(11), 1315–1329. <https://doi.org/10.1002/esp.2032>
- Wang, H., Wang, A., Bi, N., Zeng, X., & Xiao, H. (2014). Seasonal distribution of suspended sediment in the Bohai Sea, China. *Continental Shelf Research*, *90*, 17–32. <https://doi.org/10.1016/j.csr.2014.03.006>
- Wang, Z.-Y., & Liang, Z.-Y. (2000). Dynamic characteristics of the Yellow River mouth. *Earth Surface Processes and Landforms*, *25*(7), 765–782. [https://doi.org/10.1002/1096-9837\(200007\)25:7<765::AID-ESP98>3.0.CO;2-K](https://doi.org/10.1002/1096-9837(200007)25:7<765::AID-ESP98>3.0.CO;2-K)
- Warner, J. C., Sherwood, C. R., Signell, R. P., Harris, C. K., & Arango, H. G. (2008). Development of a three-dimensional, regional, coupled wave, current, and sediment-transport model. *Computers & Geosciences*, *34*(10), 1284–1306. <https://doi.org/10.1016/J.CAGEO.2008.02.012>
- Wiberg, P. L., & Rubin, D. M. (1989). Bed roughness produced by saltating sediment. *Journal of Geophysical Research*, *94*(C4), 5011. <https://doi.org/10.1029/JC094iC04p05011>
- Wilson, C. A., & Goodbred, S. L. Jr. (2015). Construction and maintenance of the Ganges-Brahmaputra-Meghna delta: Linking process, morphology, and stratigraphy. *Annual Review of Marine Science*. <https://doi.org/10.1146/annurev-marine-010213-135032>
- Wright, L. D., & Nittrouer, C. A. (1995). Dispersal of river sediments in coastal seas: Six contrasting cases. *Estuaries*, *18*(3), 494. <https://doi.org/10.2307/1352367>
- Wright, L. D., Yang, Z.-S., Bornhold, B. D., Keller, G. H., Prior, D. B., & Wiseman, W. J. (1986). Hyperpycnal plumes and plume fronts over the Huanghe (Yellow River) delta front. *Geo-Marine Letters*, *6*(2), 97–105. <https://doi.org/10.1007/BF02281645>
- Yu, L. (2002). The Huanghe (Yellow) River: A review of its development, characteristics, and future management issues. *Continental Shelf Research*, *22*(3), 389–403. [https://doi.org/10.1016/S0278-4343\(01\)00088-7](https://doi.org/10.1016/S0278-4343(01)00088-7)
- Zhang, J., Wen Huang, W., & Chong Shi, M. (1990). Huanghe (Yellow River) and its estuary: Sediment origin, transport and deposition. *Journal of Hydrology*, *120*(1–4), 203–223. [https://doi.org/10.1016/0022-1694\(90\)90150-V](https://doi.org/10.1016/0022-1694(90)90150-V)
- Zhang, P., Li, Z., & Wen, H. (2012). Modernization of national geodetic datum in China. *Nineteenth United Nations Regional Cartographic Conference for Asia and the Pacific, United Nations Economic and Social Council*, 1–6.
- Zheng, S., Wu, B., Wang, K., Tan, G., Han, S., & Thorne, C. R. (2017). Evolution of the Yellow River delta, China: Impacts of channel avulsion and progradation. *International Journal of Sediment Research*, *32*(1), 34–44. <https://doi.org/10.1016/j.ijsrc.2016.10.001>
- Zinger, J. A., Rhoads, B. L., & Best, J. L. (2011). Extreme sediment pulses generated by bend cutoffs along a large meandering river. *Nature Geoscience*, *4*(10), 675–678. <https://doi.org/10.1038/ngeo1260>